ISSN 0801-9940 No. 02
July 2013

EXPLICIT ANALYTICAL SOLUTIONS FOR HEATED, PRESSURIZED TWO-LAYER CYLINDERS

by

Knut Vedeld and Håvar A. Sollund

RESEARCH REPORT
IN MECHANICS

UNIVERSITY OF OSLO
DEPARTMENT OF MATHEMATICS
MECHANICS DIVISION

UNIVERSITETET I OSLO
MATEMATISK INSTITUTT
AVDELING FOR MEKANIKK

DEPT. OF MATH., UNIVERSITY OF OSLO
RESEARCH REPORT IN MECHANICS, No. x
ISSN 0801-9940 July 2013

EXPLICIT ANALYTICAL SOLUTIONS FOR HEATED, PRESSURIZED TWO-LAYER CYLINDERS

by

Knut Vedeld and Håvar A. Sollund

Mechanics Division, Department of Mathematics
University of Oslo, Norway

Abstract: Closed-form analytical expressions are derived for the displacement field and corresponding stress state in two-layer cylinders subjected to pressure and thermal loading. Solutions are developed both for cylinders which are fully restrained axially (plane strain) and for axially loaded and spring-mounted cylinders, assuming that the combined two-layer cross-section remains plane after deformation (generalized plane strain). It is proven formally that the classical Lamé displacement field for a pressurized thick-walled cylinder is exact for layered cylinders under generalized plane strain conditions. The analytical solutions are verified by means of detailed three-dimensional finite element analyses, and they are easily implemented in, and suitable for, engineering applications. The chosen axial boundary conditions are demonstrated to be particularly relevant for pipeline and piping applications. By applying the exact solutions derived in the present study to typical offshore lined or clad pipelines, it is demonstrated that thermal expansion of the liner or clad layer causes higher tensile hoop stresses in the pipe steel wall than accounted for in current engineering practice. Moreover, it is shown that repeated cycles of start-up and shut-down phases for lined or clad pipelines cause significant stress cycles in the liner or cladding. This may pose a risk to the integrity of such pipelines.

Keywords: Two-layer cylinder, pressure, temperature, analytical solution, pipelines, piping systems, liner, cladding

TABLE OF CONTENTS

NOMENCLATURE

A_i	$= \pi r_i^2$ [m^2]
A_o	$= \pi r_o^2$ [m^2]
$A_{o,b}$	$= \pi r_{o,b}^2$ [m^2]
A_s	Steel cross-sectional area for inner layer [m^2]
$A_{s,b}$	Steel cross-sectional area for outer layer [m^2]
$\mathbf{B}$	Unit strain matrix
C	General constant (used for strain under generalized plane strain) [-]
$\mathbf{C}[a\ ,\ b]$	Space of continuous functions on the interval $[a\ ,\ b]$
c_A	Constant to write solutions on a convenient form [-]
c_B	Constant to write solutions on a convenient form [-]
c_L	Constant to write solutions on a convenient form [-]
C_{r1}	Displacement coefficient in radial direction for the inner layer [m^2]
$C_{r1,b}$	Displacement coefficient in radial direction for the outer layer [m^2]
C_{r2}	Displacement coefficient in radial direction for the inner layer [-]
$C_{r2,b}$	Displacement coefficient in radial direction for the outer layer [-]
C_z	Displacement coefficient in axial direction for the inner layer [m]
$C_{z,b}$	Displacement coefficient in axial direction for the outer layer [m]
$\mathbf{d}$	Differential operator
$\mathbf{D}$	Displacement component vector
D_i	Internal diameter of cylinder [m]
D_o	External diameter of cylinder [m]
E	Young's modulus for the inner layer [Pa]
$\mathbf{E}$	Generalized Young's modulus [Pa]
E_b	Young's modulus for the outer layer [Pa]
$\hat{E}$	$= E / ((1 + \nu)(1 - 2\nu))$ [Pa]
$\hat{E}_b$	$= E_b / ((1 + \nu_b)(1 - 2\nu_b))$ [Pa]
k	Axial spring stiffness [N/m]
K	$= k / 2$ [N/m]
$\mathbf{K}$	Stiffness matrix
L	Length of cylinder [m]
N	Applied axial load [N]
$\mathbf{N}$	Displacement assumption matrix
$\mathbf{N_r}$	Radial displacement matrix
N_z	Axial displacement scalar [-]
P	Axial section force [N]
p_c	Contact pressure [Pa]
p_e	External pressure [Pa]
p_i	Internal pressure [Pa]
r	Radial coordinate [m]
$\mathbf{R}$	Load vector
r_i	Inner radius of combined cross-section [m]
r_o	Outer radius of inner layer [m]
$r_{o,b}$	Outer radius of outer layer [m]
S_i	Inner surface area [m^2]
S_o	Outer surface area [m^2]
t	Thickness of inner layer [m]
t_b	Thickness of outer layer [m]
$\mathbf{u}$	Displacement field vector [m]
u_r	Displacement field component in radial direction for the inner layer [m]
$u_{r,b}$	Displacement field component in radial direction the outer layer [m]
$u_{r,exact}$	Theoretical exact solution [m]
$u_{r,exp}$	Expanded displacement field for generalized solution [m]
u_z	Displacement field component in axial direction for the inner layer [m]
$u_{z,b}$	Displacement field component in axial direction for the outer layer [m]
u_θ	Displacement field component in circumferential direction for the inner layer [m]
$u_{\theta,b}$	Displacement field component in circumferential direction for the outer layer [m]
V	Volume of body [m^3]
x	Cartesian coordinate [m]
y	Cartesian coordinate [m]
z	Cartesian/cylindrical coordinate [m]
z_e	Axial coordinate of cylinder end [m]
α	Temperature expansion coefficient for inner layer [°C^{-1}]
$\alpha(r)$	Function to write solutions on a convenient form [N/m^4]
α_b	Temperature expansion coefficient for outer layer [°C^{-1}]
$\beta(r)$	Function to write solutions on a convenient form [N/m^2]
$\gamma(r)$	Function to write solutions on a convenient form [-]

γ_{ij}	Shear strains [-]
ΔT	Change in temperature [°C]
ε^0_{ij} , $\boldsymbol{\varepsilon}_0$	Tensor of initial strains [-]
ε_{ij} , $\boldsymbol{\varepsilon}$	Strain tensor for inner layer [-]
$\varepsilon_{ij,b}$	Strain tensor for outer layer [-]
θ	Circumferential coordinate [-]
ν	Poisson's ratio for inner layer [-]
ν_b	Poisson's ratio for outer layer [-]
$\rho(r)$	Theoretical error function [m]

σ^0_{ij} , $\boldsymbol{\sigma}_0$	Tensor of initial stresses [Pa]
σ_{ij} , $\boldsymbol{\sigma}$	Stress tensor for inner layer [Pa]
$\sigma_{ij,b}$	Stress tensor for outer layer [Pa]
σ_{VM}	von Mises stress [Pa]
$\overline{\sigma_{\theta\theta}}$	Mean hoop stress [Pa]
τ_{ij}	Shear stresses [Pa]
φ	Angle in axisymmetric model [-]
$\boldsymbol{\Phi}$	Surface traction vector [Pa]

1 INTRODUCTION

Solutions for stress and strain fields in heated, pressurized cylinders are a recurring theme in structural mechanics and thermoelastic investigations. Already in 1831, the French mathematician Gabriel Lamé formulated an analytical solution for the displacement field of thick-walled cylinders exposed to internal and external pressure [Lamé and Clapeyron, 1831]. The displacement field assumption in Lamé's solution may be applied to solve shrink-fit problems, as described for instance by Timoshenko [1958] for cylinders with unrestricted ends (plane stress conditions). If modified slightly, this solution can cover heating of a two-layer cylinder with different thermal expansion coefficients in the two layers. However, the assumption of plane stress requires that there is no axial interaction between the layers. The problem of pressurized thick-walled cylinders has been extended to plane strain conditions and applied to layered cylinders in a number of works, among them Eraslan and Akis [2004], Xiang et al. [2006] and Shi et al. [2007].

Corrosion, wear or diffusion resistant liners are often found in pressure vessels such as tanks, pipelines [Smith, 2012; Vedeld et al., 2012a], piping systems [Marie, 2004; Olsson and Grützner, 1989] and risers [Klowever et al., 2002]. Similar liners can be found for instance in heat exchangers [NORSOK M-001, 2004] and pressure vessels in fertilizer production [Zhang et al., 2012]. Other typical two-layer tubes include externally lined or clad cylindrical structural members [Barbezat, 2005].

Due to the frequent application of layered cylinders in industrial design, the mechanical response and thermoelastic properties of such structural members have been studied extensively. In manufacture, auto-frettage and shrink-fit techniques are highly common for production of layered cylinders, resulting in research efforts toward optimization of auto-frettage design [Focke et al., 2006; Parker, 2001; Perry and Aboudi, 2003; Wilson and Skelton, 1968]. Due to corrosion resistant liners or cladding, weight coatings, external corrosion coatings, insulation coatings etc., piping systems and offshore pipelines are always layered, and design of pipelines and piping systems rely heavily on the mechanical and thermoelastic response of cylinders, as evident from governing design codes such as the world leading offshore standard for pipelines from Det Norske Veritas, DNV-OS-F101 [2012], and the similarly dominating code for piping systems from the American Society of Mechanical Engineers, ASME B31.8 [2003]. Development of more advanced manufacturing techniques has also resulted in extensive research on the mechanical and thermoelastic response of cylinders made of functionally graded materials [Jabbari et al., 2002; Liew et al., 2002; Ootao

and Tanigawa, 2006; Xiang et al., 2006]. Functionally graded materials are characterized by material properties that are varying as a function of their spatial position. Fatigue and capacity assessment of layered cylinders subjected to thermal shock and series of micro shocks from time-dependent flow temperature and density characteristics, constitute a challenge for piping systems, particularly with multi-phase flow, as detailed by Radu et al. [2008] and Marie [2004]. Thermal loading has been treated for a variety of conditions in multi-layered cylinders. Uniform thermal stresses were applied by Akcay and Kaynak [2005], and loading from steady-state temperature distributions has been studied extensively [Jabbari et al., 2002; Shao, 2005; Zhang et al, 2012]. Time-dependent thermal stresses, both transient [Jane and Lee, 1999; Kandil et al., 1994; Lee et al., 2001, Radu et al., 2008] and cyclic [Ansari et al., 2009], have also been widely covered. Other multi-layer systems, including films, ceramics and coatings in microelectronic, optical and structural components have been studied, among others, by Hsueh [2001]. With regard to axial restraints, the studies on multi-layered or thick-walled cylinders have generally been restricted to either plane stress (no friction between the layers) [Hung et al., 2001; Jane and Lee, 1999; Lee et al., 2001; Perry and Aboudi, 2003] or plane strain conditions (no axial strain) [Akcay and Kaynak, 2005; Eraslan and Akis, 2004; Ootao and Tanigawa, 2006], or both plane stress and plane strain [Shi et al., 2006; Xiang et al., 2007].

The focus of each particular study of multi-layered cylinders varies significantly. For instance, research on auto-frettage can focus more or less solely on plastic deformation of layered sections and optimization of initial stress and strain states in the manufactured tubes with respect to intended application [Jahed et al., 2006; Parker, 2001], while research on fatigue due to transient thermal stress is generally focused on the solution of the transient thermoelastic heat equation, which in general is a more complex problem than the estimation of stresses and strains in the cylinder wall(s). Consequently, less attention has been devoted to stresses and strains in typical publications on transient thermoelastic analyses of layered cylinders, as seen for instance in the work of Radu et al. [2008] and Marie [2004]. Thus, the level of detail in the analyses range from sophisticated transient thermoelastic analyses of pressurized pipes using 3D elastic theory [Hung et al., 2001] to engineering practices with simplified steady-state temperature solutions based on the assumption of constant stress and temperature in the cylinder wall from thermal and pressure contributions [ASME B31.8, 2003].

As pointed out by Hsueh [2001], it is an intrinsic feature of multi-layer systems that the complexity in obtaining closed-form solutions increases with the number of layers. Thus,

due to the mathematical complexity of the solution algorithms and the absence of closed-form solutions, relevant studies will in some cases be unsuited for engineering purposes. Moreover, as noted by Zhang et al. [2012], many theoretical studies are neither accompanied by numerical verification, nor linked to specific applications. Furthermore, the applied boundary conditions are often of a theoretical nature and based on simplified assumptions for the stress and strain states, i.e., plane stress and plane strain as noted above. In order to apply such solutions to specific engineering problems, published solutions must, most often, be modified to better represent the problem at hand and to ensure that relevant boundary conditions are satisfied. Consequently, although the mechanical and thermoelastic response of multi-layered cylinders have been widely studied, much of the advanced research on this topic may be difficult to apply directly in engineering contexts. A strong indication that the gap between research and application is significant can be found for instance in design codes such as DNV-OS-F101 [2012] and ASME B31.8 [2003], which typically treat temperature as uniform over the cross-section, disregarding effects such as thermal shocks or steady-state variation of temperature along the pipe radius. The design codes give detailed capacity criteria for monolithic pipe cross-sections, while additional layers such as liner, cladding or concrete coating are disregarded in terms of their contribution to structural strength.

The major aim of this study is to provide exact three-dimensional, closed-form analytical solutions suitable in practical design contexts for uniformly heated, pressurized, two-layer elastic and isotropic cylinders. Various boundary conditions that are considered especially relevant for pipelines and piping systems will be included, one of which has not been treated, to the authors' knowledge, in published literature previously. In this context, the applicability of Lamé's solution field for single-layer (monolithic) cylinders to multi-layer, axially interacting cylinders will be proven formally. The study will provide novel expressions for the displacement-, stress- and strain fields of the cylinders. Since the solutions will be described on closed form, their application in engineering contexts will be straightforward and will allow for clear and transparent understanding of physical principles and system response to pressure and thermal loading.

2 PROBLEM DEFINITION

2.1 A Priori Assumptions

In this study, two-layer cylinders subjected to heat and internal and external pressure are investigated. The following basic assumptions are made a priori:

(i) The materials in the cylinder layers are assumed to be linearly elastic, homogenous and isotropic.

(ii) Initial stresses and strains from the welding and the manufacturing process are disregarded.

(iii) Bending effects are not considered. The cylinders are assumed to be perfectly straight, and the influence of curvature on the calculation of stresses due to heat and pressure is not considered.

(iv) Small displacements are assumed. Thus, the load is applied on the initial geometry, and changes in internal or external diameter and changes in layer wall thickness due to the application of loading are not accounted for.

(v) Combined, the assumptions of linear elastic material behavior and small deformations allow for the application of the principle of superposition.

(vi) The applied internal and external pressures are radial and uniformly distributed along the inner and outer surfaces of the cylinder, i.e., the pressures are treated as hydrostatic.

(vii) Heat is assumed to result in a uniform temperature distribution in the cylinder body. No temperature gradients or variations in temperature between the layers are considered.

(viii) Different cylinder layers may have different material properties, including elastic moduli, Poisson's ratios and temperature expansion coefficients.

(ix) Local stresses near pipe joints or bends due to welds or adhesive connections are not part of the investigation, i.e., the stresses are assumed to be calculated at a sufficient distance from bends or joints, such that, according to St. Venant's principle, the stress state in each cylinder layer can be considered uniformly distributed.

(x) Sections that are plane and perpendicular to the cylinder axis prior to deformation are assumed to remain plane and perpendicular to the cylinder axis after

deformation. This is reasonable since the considered cylinders represent short segments of long pipelines or piping systems with cross-sections consisting of layers that are axially fixed to each other, either continuously or at regular intervals (i.e., end effects are ignored and relative sliding between layers will not occur).

2.2 Coordinate System

The standard cylindrical coordinate system defined in Figure 1 is adopted in the present study.

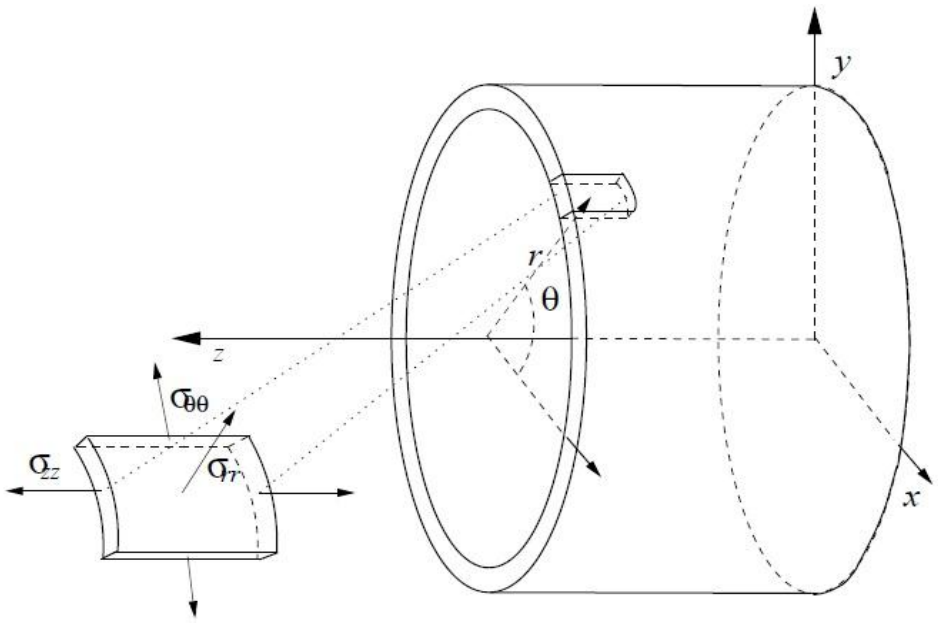

Figure 1 – Cylindrical coordinate system and stress nomenclature.

In the figure, x, y and z are the standard Cartesian coordinates, r is the radial coordinate, θ is the angle between the position vector and the x-axis, σ_{rr} is the radial stress, σ_{zz} is the axial stress and $\sigma_{\theta\theta}$ is the hoop stress.

2.3 Boundary Conditions

An illustration of the cross-section and static radial boundary conditions of the two-layer cylinder problem is shown in Figure 2. In the figure, p_e is the external pressure, p_i is the internal pressure, r_i is the internal radius of the inner cylinder layer, r_o is the outer radius of the inner cylinder layer and $r_{o,b}$ is the outer radius of the outer cylinder layer.

On the inner surface, the radial stress must be compressive and equal to the internal pressure, resulting in a static radial boundary condition given by

$$\sigma_{rr}(r_i) = -p_i \quad \textbf{(1)}$$

Similarly, the static radial boundary condition on the outer surface is given by

$$\sigma_{rr,b}(r_{o,b}) = -p_e \quad \textbf{(2)}$$

where $\sigma_{rr,b}$ is the radial stress in the outer layer.

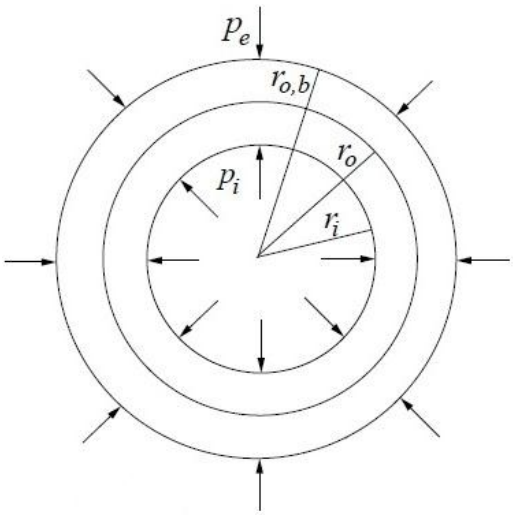

Figure 2 – Cross-section of a two-layer cylinder with internal and external pressure.

Kinematic boundary conditions and static axial boundary conditions (axial loading) are displayed in Figure 3. In the figure, arrow heads indicate translational constraints and double arrow heads indicate rotational constraints. Each of the cylinders a) and b) represents a segment, or cut-out, of a long pipe. The considered cylinders have length L and are assumed free to expand or contract radially. There are no end-caps. Cylinder a) in the figure is fully restrained axially. The boundary condition is thus characterized by plane strain, with a mathematical representation defined by

$$\varepsilon_{zz} = 0 \quad \textbf{(3)}$$

where ε_{zz} is the strain in axial direction. Hence, the axial strain is known, while the axial reaction load is unknown. As mentioned previously, solutions for this particular boundary condition do exist in the literature, but to the authors' knowledge not in closed form for the two-layer case with uniform thermal loads included.

For the second boundary condition, illustrated by cylinder b) in the figure, the cylinder is fully restrained at only one end (z = 0). At the opposite end (z = L), the cylinder may

expand axially, but the cross-section must remain plane in accordance with assumption (x) (Section 2.1). This is visualized in Figure 3 b) by a kinematic coupling, indicated by dashed lines, between a reference point (RP) and the cylinder end surface. Thus, the cylinder is in a state of generalized plane strain, defined by

$$\varepsilon_{zz} = C \tag{4}$$

where C is a non-zero constant. The constant C will have the same value in both layers.

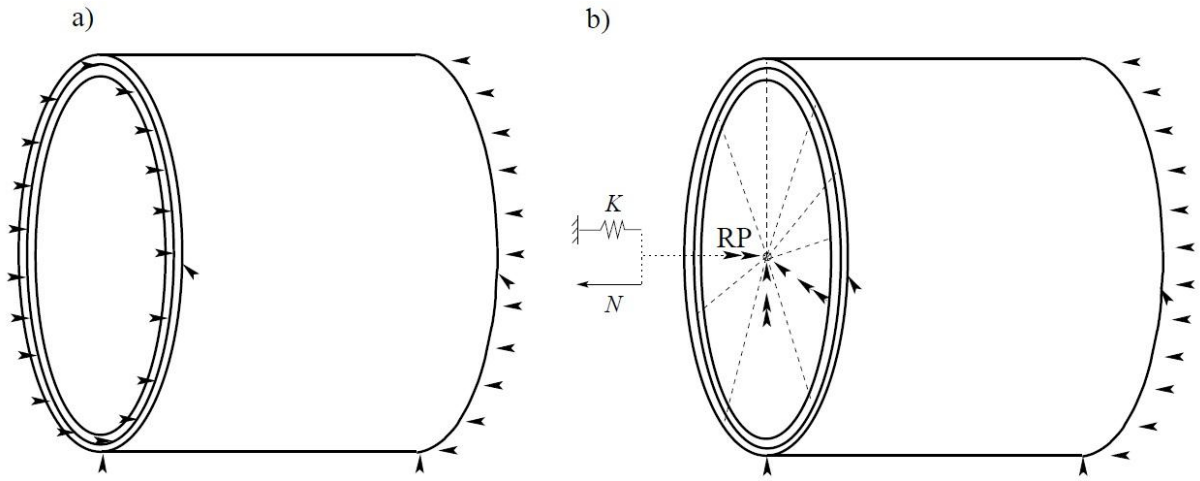

Figure 3 – Boundary conditions for: a) the axially fixed condition and b) the axially free condition. Arrow heads indicate translational and double arrow heads rotational constraints.

An axial load N and an axial spring with stiffness K are applied at the reference point (RP). It should be noted that N is an applied load, and integration of the axial stresses σ_{zz} (in the inner layer) and $\sigma_{zz,b}$ (in the outer layer) over the cross-section would generally give a result that is different from N. A static equilibrium equation in z-direction may be formulated at $z = L$ for the cylinder in Figure 3 b). The equilibrium equation is given by

$$\sigma_{zz}A_s + \sigma_{zz,b}A_{s,b} = -K \cdot u_z(L) + N, \tag{5}$$

where $A_s = \pi t(2r_o - t)$ is the cross-sectional area of the inner layer, $A_{s,b} = \pi t_b(2r_{o,b} - t_b)$ is the cross-sectional area of the outer layer, and $u_z(L)$ is the axial displacement at $z = L$.

2.4 Boundary Conditions for Piping and Pipelines

In order to identify relevant boundary conditions for pipes and piping, it is useful to consider a typical piping or pipeline scenario, as illustrated by Figure 4. In Figure 4 c), a segment, or cut-out, of a piping system (Figure 4 a) or pipeline (Figure 4 b) is shown. Regardless of whether the cut-out is taken from a pipeline or a piping system, some axial

stiffness is provided by axial interaction with the rest of the system. In addition, for subsea pipelines that are resting on the seabed, the axial friction is often modeled by springs with axial stiffness dependent on the soil type. Hence, spring stiffness is introduced in axial direction. However, in many cases the action on a pipe segment by its surroundings is represented by an applied load N rather than by axial springs. For example, at lay-down (i.e., just after installation) a subsea pipeline will have a residual lay tension and some non-zero axial strain, which implies that the pipe segment should be modeled with an external load N and no spring stiffness. When operational loads subsequently are applied, the degree of axial restraint may vary from zero (close to a spool or other flexible structure) to fully fixed (when the accumulated soil friction is large enough to fully restrain the pipe). For axial restraints in-between zero and full fixation, the pipe segment may be modeled with axial springs. The spring stiffness will depend on e.g., the stiffness properties of the soil and the length L of the considered pipe segment. Thus, in order to facilitate the different manners of modeling the pipe segment's interaction with its surroundings, the problem has been idealized as shown in Figure 4 c). In the figure, an axial section force P acts on both ends of the pipe segment and includes potential contributions from both a spring force and an applied axial load. The section force may be expressed by

$$P = -k \cdot u_z(z_e) + N, \tag{6}$$

where $u_z(z_e)$ denotes the axial displacement of either cylinder end.

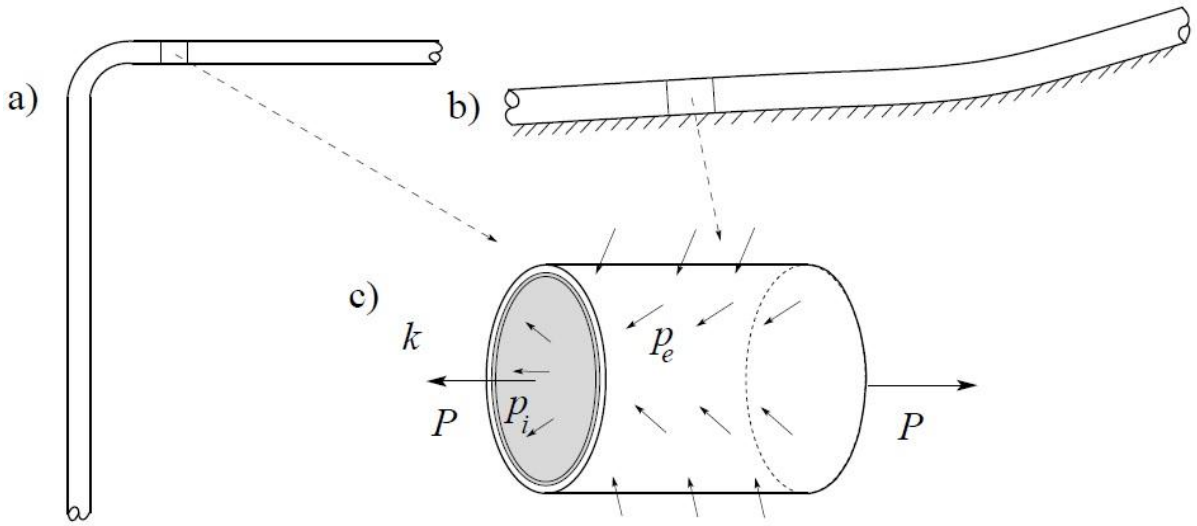

Figure 4 –a) Typical part of a two layer piping system configuration. b) Typical scenario for a two layer submarine pipeline resting on the seabed. c) Model of a pipe segment applicable to both scenario a) and scenario b).

From Eq. (6), one may observe that there is a spring with stiffness k mounted to each end of the pipe segment in Figure 4 c). It should be noted that the system in Figure 4 c) corresponds to the system in Figure 3 a) when $k \to \infty$. Moreover, the system in Figure 4 c) may be retrieved from the system in Figure 3 b) by setting $K = k/2$, or by setting $K = k$ while adjusting the length of the cylinder from L to $L/2$. The latter is evident from symmetry. Thus, the boundary conditions for the pipe segment in Figure 4 c) are equivalent to the boundary conditions illustrated previously by Figure 3.

3 DISPLACEMENT ASSUMPTIONS

3.1 Short Historical Background

A brief introduction to the classical theory of pressurized cylinders is presented in this section. It may be found in several textbooks on strength of materials, e.g., Timoshenko [1958], but is included here for completeness and for ease-of-reference in the subsequent novel derivations for solutions to the problem of heated and pressurized two-layer cylinders.

Figure 5 shows a cylinder with uniform internal and external pressures acting along its inner and outer circumferences. The mean hoop stress may be calculated as

$$\overline{\sigma_{\theta\theta}} = \frac{\int_0^{\pi} (p_i r_i - p_e r_o) \sin\theta \, d\theta}{2t} = \frac{p_i D_i - p_e D_o}{2t} \tag{7}$$

where D_i is the internal diameter, D_o the outer diameter and t is the wall thickness of the cylinder wall.

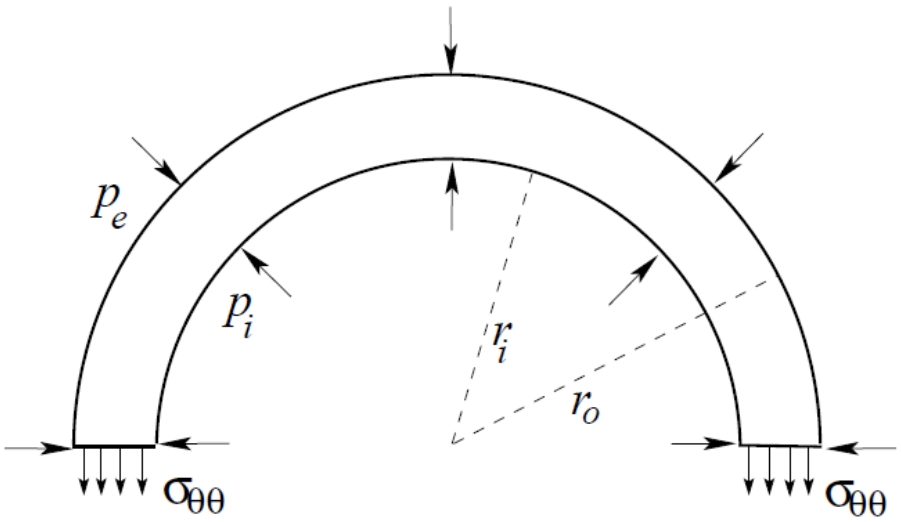

Figure 5 – Pressures and approximate stresses in a thin walled cylinder intersected along a random diameter line.

Eq. (7) is often sufficient for estimating the hoop stress in a pressurized ring or cylinder, especially when the wall thickness t is small compared to the mean diameter $\overline{D}$. However, for a thick-walled cylinder, the radial stress is non-negligible, and the hoop stress is non-uniform over the cross-section. It is then of interest to know the exact radial distribution of the radial stresses and hoop stresses. Since the internal and external pressures are uniformly distributed along the circumference, the resulting deformation will be symmetric about the

axis of the cylinder. This requires the hoop displacement to become zero, i.e., $u_\theta = 0$. Moreover, the symmetry implies that the shearing stresses $\tau_{r\theta}$ are zero. The shearing stresses τ_{rz} will also be zero since the thermal loading and pressures are uniform in axial direction, and the axial displacements according to assumption (x) (Section 2.1) are constant over the cross-section. The conditions for equilibrium in radial direction may consequently be derived based on Figure 6, which displays the radial and hoop stresses acting on an infinitesimal element in a plane perpendicular to the cylinder axis (*z*-axis).

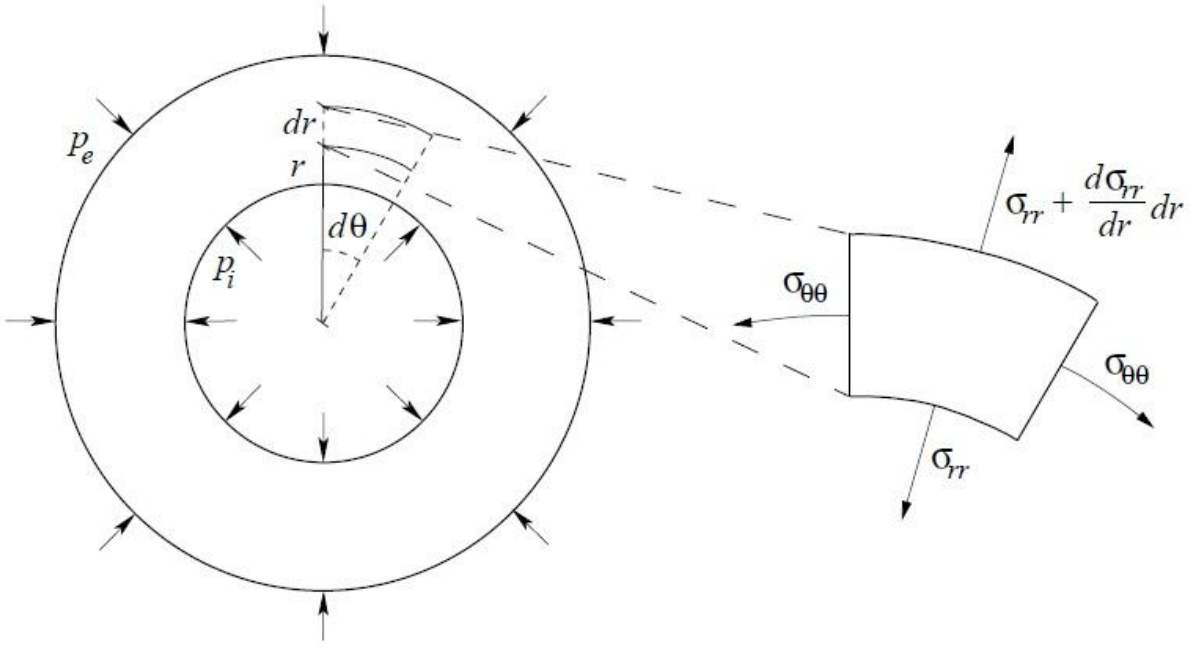

Figure 6 - A thick-walled ring (cylinder) subject to internal and external pressure and resulting stresses.

Noting that $\sin(d\theta) \approx d\theta$ and disregarding the body force, the following equilibrium equation can be formulated in the radial direction for the element:

$$\sigma_{rr} r d\theta + \sigma_{\theta\theta} dr d\theta - \left(\sigma_{rr} + \frac{d\sigma_{rr}}{dr} dr \right)(r + dr) d\theta = 0 \qquad \textbf{(8)}$$

By ignoring higher-order quantities one obtains

$$\sigma_{\theta\theta} - \sigma_{rr} - r \frac{d\sigma_{rr}}{dr} = 0 \qquad \textbf{(9)}$$

Let us assume that the cylinder displayed in Figure 6 is free to expand in the axial direction. The axial stresses will be zero, and the cylinder will be in a condition of plane stress. Hooke's material law for plane stress is given by

$$\begin{bmatrix}\sigma_{rr}\\ \sigma_{\theta\theta}\end{bmatrix}=\frac{E}{1-\nu^2}\begin{bmatrix}1 & \nu\\ \nu & 1\end{bmatrix}\begin{bmatrix}\varepsilon_{rr}\\ \varepsilon_{\theta\theta}\end{bmatrix} \tag{10}$$

where E is the Young's modulus and ν the Poisson's ratio for the cylinder wall material. The radial strain is defined as

$$\varepsilon_{rr}=\frac{du_r}{dr} \tag{11}$$

Since there is no displacement u_θ in the circumferential direction, the only contribution to elongation in the circumferential direction will be due to the change in radius resulting from the radial displacement u_r. Consequently, the hoop strain will be given by

$$\varepsilon_{\theta\theta}=\frac{2\pi(r+u_r)-2\pi r}{2\pi r}=\frac{u_r}{r} \tag{12}$$

By inserting the stress expressions from Eq. (10) into Eq. (9), the following differential equation for the radial displacement u_r is obtained:

$$\frac{d^2u_r}{dr^2}+\frac{1}{r}\frac{du_r}{dr}-\frac{u_r}{r^2}=0 \tag{13}$$

The general solution of the differential equation is

$$u_r=\frac{C_{r1}}{r}+C_{r2}r \tag{14}$$

which may be verified by substitution. The two coefficients C_{r1} and C_{r2} may be obtained from the boundary conditions at the inner and outer cylinder surfaces, where the pressures must be balanced by the radial stresses:

$$\sigma_{rr}(r_i)=-p_i \quad \text{and} \quad \sigma_{rr}(r_o)=-p_e \tag{15}$$

By making use of Eqs. (11), (12) and (14), the radial and hoop stresses in Eq. (10) may be expressed as

$$\begin{aligned}\sigma_{rr}(r)&=\frac{E}{1-\nu^2}\left(-(1-\nu)\frac{C_{r1}}{r^2}+(1+\nu)C_{r2}\right)\\ \sigma_{\theta\theta}(r)&=\frac{E}{1-\nu^2}\left((1-\nu)\frac{C_{r1}}{r^2}+(1+\nu)C_{r2}\right)\end{aligned} \tag{16}$$

From Eqs. (15) and (16) the following expressions are obtained for the displacement field coefficients:

$$\begin{aligned}C_{r1}&=\frac{1+\nu}{E}\frac{r_i^2r_o^2(p_i-p_e)}{r_o^2-r_i^2}\\ C_{r2}&=\frac{1-\nu}{E}\frac{r_i^2p_i-r_o^2p_e}{r_o^2-r_i^2}\end{aligned} \tag{17}$$

The final expression for the stresses in the cylinder then becomes

$$\sigma_{rr}(r) = -\frac{(p_i - p_e) r_i^2 r_o^2}{r^2 (r_o^2 - r_i^2)} + \frac{p_i r_i^2 - p_e r_o^2}{r_o^2 - r_i^2}$$
$$\sigma_{\theta\theta}(r) = \frac{(p_i - p_e) r_i^2 r_o^2}{r^2 (r_o^2 - r_i^2)} + \frac{p_i r_i^2 - p_e r_o^2}{r_o^2 - r_i^2} \quad \textbf{(18)}$$

This solution for radial and hoop stresses in a pressurized cylinder was first published by Lamé and Clapeyron [1831]. The general displacement field described by Eq. (14) will often be referred to as the Lamé displacement field in the present study.

It should be noted that the sum of radial and hoop stresses taken from Eq. (18) is constant, i.e., independent of *r*, and given by

$$\sigma_{rr} + \sigma_{\theta\theta} = \frac{2(p_i r_i^2 - p_e r_o^2)}{r_o^2 - r_i^2} \quad \textbf{(19)}$$

This is a notable result. While each of the stress components vary (with the radius) over the wall thickness, and therefore produce, due to the Poisson effect (lateral expansion), axial strains that vary over the wall thickness, the axial strains from the sum of the two components will be constant. This justifies a two-dimensional treatment of the problem, since cross-sections that are plane and perpendicular to the cylinder axis before deformation, will remain plane and perpendicular to the axis after deformation.

The differential equation for the radial displacement, Eq. (13), was derived above under the assumption of plane stress. However, it is straight-forward to show that the same differential equation will be obtained by assuming zero strain in the axial direction (i.e., plane strain condition). Eq. (10) must then be replaced by Hooke's material law for plane strain, given by

$$\begin{bmatrix} \sigma_{rr} \\ \sigma_{\theta\theta} \end{bmatrix} = \frac{E}{(1+\nu)(1-2\nu)} \begin{bmatrix} 1-\nu & \nu \\ \nu & 1-\nu \end{bmatrix} \begin{bmatrix} \varepsilon_{rr} \\ \varepsilon_{\theta\theta} \end{bmatrix} \quad \textbf{(20)}$$

The strains may again be expressed in terms of the radial displacement by using Eqs. (11) and (12), and inserted into the plane strain material law, Eq. (20). By inserting the resulting stresses into the equilibrium equation, Eq. (9), one obtains, as mentioned above, the same differential equation, Eq. (13), as was found in the plane stress case. Hence, the general solution given in Eq. (14) applies for both plane stress and plane strain. The boundary conditions in Eq. (15) still apply, and it can easily be shown that the displacement field coefficients will be

$$C_{r1} = \frac{1+\nu}{E}\frac{r_i^2 r_o^2 (p_i - p_e)}{r_o^2 - r_i^2}$$
$$C_{r2} = \frac{(1+\nu)(1-2\nu)}{E}\frac{r_i^2 p_i - r_o^2 p_e}{r_o^2 - r_i^2} \quad \textbf{(21)}$$

It is seen, when comparing to the plane stress solution, Eq. (17), that the expressions for C_{r1} are identical. This is not the case for the C_{r2} coefficients.

3.2 Displacement Field for Two-Layer Cylinders Subjected to Radial Pressure, Temperature and Axial Loading

In this section, direct axial loading and temperature are considered in addition to uniform radial pressure along the inner and outer circumferences of a cylinder. As described in Section 2.3, two different axial boundary conditions are considered. They are repeated below for ease-of-reference:

1) Fully restrained ends (plane strain condition), which can be represented mathematically by $\varepsilon_{zz} = 0$ for both layers.
2) Free end with axial load N and axial spring stiffness K and no relative sliding between the layers (generalized plane strain condition), which can be represented mathematically by $\varepsilon_{zz} = C$, where the constant C is the same for both layers.

Boundary condition 1) corresponds to the plane strain condition which was discussed in Section 3.1. Compared to the discussion in Section 3.1, there are two notable differences. Firstly, the cross-section consists of two layers with different Young's moduli, Poisson's ratios and temperature expansion coefficients (denoted α in the inner layer and α_b in the outer layer). Secondly, the cylinder is subjected to a uniform temperature change. Due to the difference in temperature expansion coefficients between the layers, a positive thermal load will induce a compressive contact force (i.e., a contact pressure) on the layer interface if $\alpha > \alpha_b$, and conversely, a tensile contact force (a negative contact pressure) will be induced if $\alpha < \alpha_b$. For all practical purposes with regard to pipelines and piping, the inner layer (i.e., the liner or cladding) will have the larger temperature expansion coefficient, so the contact force will in the following be termed "the contact pressure" and denoted p_c. Thus, for boundary condition 1), each layer in the two-layer cross-section may be regarded as a pressurized cylinder under plane strain conditions. The inner layer will be subjected to an internal

pressure p_i and an external pressure p_c, while the outer layer will be subjected to an internal pressure equal to p_c, and an external pressure p_e. Consequently, as shown for the plane-strain case in Section 3.1, the radial displacement field will for each layer be given by Eq. (14).

For boundary condition 2), in addition to the introduction of a contact pressure p_c between the layers, a pure (and positive) thermal load will induce a non-zero axial strain, accompanied by a compressive axial stress in the layer with the larger temperature expansion coefficient, and a tensile axial stress in the other layer. Since both the axial strain and the axial stress will be non-zero in each of the two layers, the results for pressurized cylinders under plane strain and plane stress conditions in Section 3.1 are not directly applicable. However, it may be argued that the radial equilibrium equation, Eq. (9), is still valid. If this is so, it is straight-forward to apply Hooke's three-dimensional material law, which is given later by Eq. (32), and insert the relevant expressions for radial stress σ_{rr} and hoop stress $\sigma_{\theta\theta}$ into Eq. (9). The resulting relation becomes

$$-(1-2\nu)\varepsilon_{rr}+(1-2\nu)\varepsilon_{\theta\theta}-r(1-\nu)\frac{d\varepsilon_{rr}}{dr}-r\nu\frac{d\varepsilon_{\theta\theta}}{dr}-r\nu\frac{d\varepsilon_{zz}}{dr}=0 \qquad \textbf{(22)}$$

Since sections that are plane and perpendicular to the cylinder axis prior to deformation are assumed to remain plane and perpendicular to the cylinder axis after deformation, it follows that

$$\frac{d\varepsilon_{zz}}{dr}=0 \qquad \textbf{(23)}$$

By using Eqs. (11) and (12) to express the radial and circumferential strains in terms of the radial displacement u_r, Eq. (22) becomes identical to the differential equation, Eq. (13), for u_r obtained in Section 3.1. Thus, the radial displacement field will for each layer be given by Eq. (14) also for the case of generalized plane strain.

The argument in the preceding paragraph is based on the assumption that the equilibrium equation in radial direction, Eq. (9), is valid for each layer even when the strain and stress states are three-dimensional. This assumption is generally adopted in the literature, both for cross-sections with radially varying material properties [Jabbari et al., 2002; Peng and Li, 2010; Zhang et al., 2012] and for axially loaded cylinders [Ansari et al., 2010; Tarn and Wang, 2000]. However, the authors of the present study are not aware of any rigorous investigation of its validity for the particular case of a two-layer cylinder under generalized plane-strain conditions, subjected to both direct axial loading and temperature in addition to uniform radial pressure. For this reason, it is demonstrated by a formal mathematical proof in

Appendix A that the Lamé displacement field, Eq. (14), indeed is applicable for each cylinder layer, as argued in the preceding paragraph.

With regard to the two remaining displacement components, it should be noted that since the problem is axisymmetrical, the circumferential displacement u_θ is zero. This applies for both axial boundary conditions. For boundary condition 1), the axial displacement u_z must also, by definition, be zero. For boundary condition 2), on the other hand, the differential equation for the axial displacement follows directly from Eq. (4) in conjunction with the definition of the axial strain:

$$\left.\begin{aligned} \varepsilon_{zz} &= \frac{du_z}{dz} \\ \varepsilon_{zz} &= C \end{aligned}\right\} \quad \Rightarrow \quad \frac{du_z}{dz} = C \tag{24}$$

Solving Eq. (24) with respect to the boundary conditions in Figure 3 b) yields the following displacement field in axial direction:

$$u_z = C_z \frac{z}{L} \tag{25}$$

where C_z is a constant.

Based on the above, the full displacement field for each layer (applicable for both boundary conditions) may be written as

$$\begin{aligned} u_r &= \frac{C_{r1}}{r} + C_{r2} r \\ u_\theta &= 0 \\ u_z &= C_z \frac{z}{L} \end{aligned} \tag{26}$$

In the following, the nomenclature in Eq. (26) is adopted for the inner layer. For the outer layer, the same notation, but with the addition of a subscript "*b*" after each entity, will be used. For instance, the radial displacement field becomes $u_{r,b}$ and the second displacement coefficient in radial direction (the linear term) becomes $C_{r2,b}$. In the axial direction, $C_z = 0$ for plane strain and $C_{z,b} = C_z$ for the generalized plane strain conditions.

4 STRESS AND STRAIN RELATIONS

The cylindrical coordinate system presented in Figure 1 will be applied throughout. The strain field in cylindrical coordinates [Cook et al. 2002] may be derived from the displacement field given by Eq. (26). The resulting strains become as follows:

$$\begin{aligned}
\varepsilon_{rr} &= \frac{\partial u_r}{\partial r} = -\frac{C_{r1}}{r^2} + C_{r2} \\
\varepsilon_{\theta\theta} &= \frac{1}{r}\frac{\partial u_\theta}{\partial \theta} + \frac{1}{r}u_r = \frac{C_{r1}}{r^2} + C_{r2} \\
\varepsilon_{zz} &= \frac{\partial u_z}{\partial z} = \frac{C_z}{L} \\
\gamma_{r\theta} &= \frac{1}{r}\frac{\partial u_r}{\partial \theta} + \frac{\partial u_\theta}{\partial r} - \frac{u_\theta}{r} = 0 \\
\gamma_{\theta z} &= \frac{\partial u_\theta}{\partial z} + \frac{1}{r}\frac{\partial u_z}{\partial \theta} = 0 \\
\gamma_{rz} &= \frac{\partial u_r}{\partial z} + \frac{\partial u_z}{\partial r} = 0
\end{aligned} \tag{27}$$

The shear strains are all zero, as expected from the symmetry of the problem. Again, a subscript "*b*" will be applied to indicate that a variable belongs to the outer layer. For instance $\varepsilon_{rr,b}$ will denote the radial strain in the outer layer, whereas no subscript indicates the inner layer. Since the shear strains vanish, the strain tensor may be represented by

$$\boldsymbol{\varepsilon} = \begin{bmatrix} \varepsilon_{rr} \\ \varepsilon_{\theta\theta} \\ \varepsilon_{zz} \end{bmatrix} = \begin{bmatrix} \dfrac{\partial u_r}{\partial r} \\ \dfrac{u_r}{r} \\ \dfrac{\partial u_z}{\partial z} \end{bmatrix} \tag{28}$$

The effect of a thermal loading (i.e., an increase or decrease in temperature) can either be accounted for through an initial stress or an initial strain. In this study, it is chosen to apply the thermal loadings as initial strains. The constitutive stress-strain relationship, taking these initial strains into account, can then be written

$$\boldsymbol{\sigma} = \mathbf{E}\left(\boldsymbol{\varepsilon} - \boldsymbol{\varepsilon}_0\right) + \boldsymbol{\sigma}_0 \tag{29}$$

where $\boldsymbol{\sigma}_0 = \mathbf{0}$. The initial strains in the cylinder layers are found by linear temperature expansion:

$$\varepsilon_{rr}^0 = \varepsilon_{\theta\theta}^0 = \varepsilon_{zz}^0 = \alpha \Delta T \tag{30}$$

In Eq. (30), α is the temperature expansion coefficient, ΔT is the relative change in temperature, and the superscripts "0" are included in order to indicate that they are initial strains. The generalized Young's modulus **E** in Eq. (29) is given by

$$\mathbf{E} = \hat{E}\begin{bmatrix} 1-\nu & \nu & \nu \\ \nu & 1-\nu & \nu \\ \nu & \nu & 1-\nu \end{bmatrix}, \quad \text{where} \quad \hat{E} = \frac{E}{(1-2\nu)(1+\nu)} \tag{31}$$

In the absence of shear strains, the full three-dimensional stress state in the inner layer of the two-layer cylinder is thus given by

$$\begin{bmatrix} \sigma_{rr} \\ \sigma_{\theta\theta} \\ \sigma_{zz} \end{bmatrix} = \hat{E}\begin{bmatrix} 1-\nu & \nu & \nu \\ \nu & 1-\nu & \nu \\ \nu & \nu & 1-\nu \end{bmatrix}\begin{bmatrix} \frac{\partial u_r}{\partial r} - \alpha\Delta T \\ \frac{u_r}{r} - \alpha\Delta T \\ \frac{\partial u_z}{\partial z} - \alpha\Delta T \end{bmatrix}, \tag{32}$$

where σ_{rr} is the radial stress, $\sigma_{\theta\theta}$ is the hoop stress, and σ_{zz} is the axial stress in the inner cylinder layer. For the outer layer, the same symbols are used, albeit with a subscript "*b*" added. After inserting for the displacement field, Eq. (26), into Eq. (32), the stress field becomes

$$\begin{bmatrix} \sigma_{rr} \\ \sigma_{\theta\theta} \\ \sigma_{zz} \end{bmatrix} = \hat{E}\begin{bmatrix} -(1-2\nu)\frac{C_{r1}}{r^2} + C_{r2} + \nu\frac{C_z}{L} - \alpha\Delta T(1+\nu) \\ (1-2\nu)\frac{C_{r1}}{r^2} + C_{r2} + \nu\frac{C_z}{L} - \alpha\Delta T(1+\nu) \\ 2\nu C_{r2} + (1-\nu)\frac{C_z}{L} - \alpha\Delta T(1+\nu) \end{bmatrix} \tag{33}$$

As noted in conjunction with Eq. (26), this formulation covers both the axial boundary conditions, with only the coefficient C_z becoming different in each case.

Interestingly, one may observe from Eq. (33) that

$$\frac{\sigma_{rr} + \sigma_{\theta\theta}}{2} = C_{r2} + \nu\frac{C_z}{L} - \alpha\Delta T(1+\nu) \tag{34}$$

In other words, the sum of the radial and hoop stresses is generally independent of the radial coordinate *r*, as was demonstrated previously for a single-layer thick-walled cylinder, subject only to internal and external pressure. Thus, it can be concluded that the radial independence is valid also for the sum of hoop and radial stresses in each layer of a two-layer cylinder under plane strain and generalized plane strain conditions.

Since there are no shear stresses, the radial, hoop and axial stresses given by Eq. (33) are also the principal stresses. In order to predict whether a material will yield under

multiaxial loading conditions, it is convenient to define the von Mises stresses, given in terms of principal stresses by

$$\sigma_{VM} = \sqrt{\frac{(\sigma_{rr} - \sigma_{\theta\theta})^2 + (\sigma_{\theta\theta} - \sigma_{zz})^2 + (\sigma_{rr} - \sigma_{zz})^2}{2}} \,. \quad \textbf{(35)}$$

According to the commonly applied von Mises yield criterion, yield will occur when the von Mises stress exceeds the yield stress of the material.

5 ANALYTICAL SOLUTIONS

5.1 Pressurized Two-Layer Cylinder under Plane Strain Conditions

The first boundary condition considered is that of the axially fixed cylinder, as defined in Figure 3 a). As seen from Eqs. (26) and (33), the displacement fields and stress states of the inner and the outer layer contain six undetermined coefficients (C_{r1}, C_{r2}, C_z, $C_{r1,b}$, $C_{r2,b}$ and $C_{z,b}$). The coefficients for the axial displacement are easily determined. Since the cylinder is fixed axially, they are both zero:

$$C_z = C_{z,b} = 0 \tag{36}$$

As noted in Section 2.3, the radial stress at the inner surface equals the internal pressure and the radial stress at the outer surface equals the external pressure. Thus,

$$\begin{aligned} \sigma_{rr}(r_i) &= -p_i \\ \sigma_{rr,b}(r_{o,b}) &= -p_e \end{aligned} \tag{37}$$

The displacement field must be continuous at the interface between the cylinder layers:

$$u_r(r_o) = u_{r,b}(r_o) \tag{38}$$

Finally, the contact pressure between the surfaces must equal the radial stress at the interface. Consequently, the radial stresses must be equal at the contact surface:

$$\sigma_{rr}(r_o) = \sigma_{rr,b}(r_o) \tag{39}$$

Combining Eqs. (33) and (36) - (39), the following system of equations can be established for the undetermined coefficients:

$$\begin{bmatrix} -\frac{\hat{E}(1-2\nu)}{r_o^2} & \hat{E} & \frac{\hat{E}_b(1-2\nu_b)}{r_o^2} & -\hat{E}_b \\ \frac{1}{r_o} & r_o & -\frac{1}{r_o} & -r_o \\ -\frac{(1-2\nu)}{r_i^2} & 1 & 0 & 0 \\ 0 & 0 & -\frac{(1-2\nu_b)}{r_{o,b}^2} & 1 \end{bmatrix} \begin{bmatrix} C_{r1} \\ C_{r2} \\ C_{r1,b} \\ C_{r2,b} \end{bmatrix} = \begin{bmatrix} 0 \\ 0 \\ -\frac{p_i}{\hat{E}} \\ -\frac{p_e}{\hat{E}_b} \end{bmatrix} \tag{40}$$

Solving the system of equations in Eq. (40) yields the following analytical expressions for the displacement field coefficients of the inner and outer cylinders:

$$C_{r1}=\frac{K_{22}R_1-K_{12}R_2}{K_{11}K_{22}-K_{12}K_{21}} \quad \text{and} \quad C_{r2}=-\frac{p_i}{\hat{E}}+\frac{1-2\nu}{r_i^2}C_{r1}\,,$$
$$C_{r1,b}=\frac{-K_{21}R_1+K_{11}R_2}{K_{11}K_{22}-K_{12}K_{21}} \quad \text{and} \quad C_{r2,b}=-\frac{p_e}{\hat{E}_b}+\frac{1-2\nu_b}{r_{o,b}^2}C_{r1,b}\,, \tag{41}$$

where

$$K_{11}=\hat{E}(1-2\nu)\left(\frac{1}{r_i^2}-\frac{1}{r_o^2}\right) \quad \text{and} \quad K_{12}=\hat{E}_b(1-2\nu_b)\left(\frac{1}{r_o^2}-\frac{1}{r_{o,b}^2}\right),$$
$$K_{21}=\frac{1}{r_o^2}+\frac{1-2\nu}{r_i^2} \quad \text{and} \quad K_{22}=-\frac{1}{r_o^2}-\frac{1-2\nu_b}{r_{o,b}^2}\,, \tag{42}$$
$$R_1=p_i-p_e \quad \text{and} \quad R_2=\frac{p_i}{\hat{E}}-\frac{p_e}{\hat{E}_b}\,.$$

5.2 Pressurized and Axially Loaded Two-Layer Cylinder under Generalized Plane Strain Conditions

The second boundary condition investigated is taken according to the spring-mounted configuration in Figure 3 b). Like in the previous Section 5.1, six coefficients must be determined in order to fully describe the displacement fields and stress states of the two cylinder layers. Eqs. (37), (38) and (39) still apply for the spring-mounted system. This yields four equations in six unknowns. The last two equations can be found from continuity of axial displacements near the spring mount at $z = L$, and from the equilibrium of spring load, axial load and axial stresses at $z = L$, which was previously discussed in Section 2.3.

The axial displacements in the two layers must be equal, in accordance with Eq. (4). Consequently, we obtain the following equation:

$$u_z(L)=u_{z,b}(L) \quad \Rightarrow \quad C_z=C_{z,b} \tag{43}$$

The static equilibrium equation in the axial direction near the spring mount is given by Eq. (5), which is repeated below for ease-of-reference:

$$\sigma_{zz}A_s+\sigma_{zz,b}A_{s,b}=-K\cdot u_z(L)+N=-KC_z+N\,, \tag{44}$$

where A_s is the cross-sectional area of the inner cylinder layer, and $A_{s,b}$ is the cross-sectional area of the outer cylinder layer.

Combining Eqs. (33), (37), (38), (39), (43) and (44) yields a system of five equations for the undetermined field coefficients, given by

$$\begin{bmatrix} -\frac{\hat{E}(1-2\nu)}{r_o^2} & \hat{E} & \frac{\hat{E}\nu-\hat{E}_b\nu_b}{L} & \frac{\hat{E}_b(1-2\nu_b)}{r_o^2} & -\hat{E}_b \\ \frac{1}{r_o} & r_o & 0 & -\frac{1}{r_o} & -r_o \\ -\frac{(1-2\nu)}{r_i^2} & 1 & \frac{\nu}{L} & 0 & 0 \\ 0 & 0 & \frac{\nu_b}{L} & -\frac{(1-2\nu_b)}{r_{o,b}^2} & 1 \\ 0 & 2\nu\hat{E}A_s & \frac{\hat{E}A_s(1-\nu)+\hat{E}_bA_{s,b}(1-\nu_b)}{L}+K & 0 & 2\nu_b\hat{E}_bA_{s,b} \end{bmatrix} \begin{bmatrix} C_{r1} \\ C_{r2} \\ C_z \\ C_{r1,b} \\ C_{r2,b} \end{bmatrix} = \begin{bmatrix} 0 \\ 0 \\ -\frac{p_i}{\hat{E}} \\ -\frac{p_e}{\hat{E}_b} \\ N \end{bmatrix} \quad \textbf{(45)}$$

The solution of this system of equations gives the following closed expression for the field equation coefficients:

$$\begin{aligned} &C_{r1}=\frac{K_{22}R_1-K_{12}R_2}{K_{11}K_{22}-K_{12}K_{21}} \quad \text{and} \quad C_{r1,b}=\frac{-K_{21}R_1+K_{11}R_2}{K_{11}K_{22}-K_{12}K_{21}}, \\ &C_z=\frac{L}{\nu_b-\nu}\left(\frac{p_i}{\hat{E}}-\frac{p_e}{\hat{E}_b}-C_{r1}\frac{r_i^2+r_o^2(1-2\nu)}{r_i^2r_o^2}+C_{r1,b}\frac{r_{o,b}^2+r_o^2(1-2\nu_b)}{r_{o,b}^2r_o^2}\right), \\ &C_{r2}=-\frac{p_i}{\hat{E}}+\frac{1-2\nu}{r_i^2}C_{r1}-\frac{\nu}{L}C_z \quad \text{and} \quad C_{r2,b}=-\frac{p_e}{\hat{E}_b}+\frac{1-2\nu_b}{r_{o,b}^2}C_{r1,b}-\frac{\nu_b}{L}C_z, \end{aligned} \quad \textbf{(46)}$$

where

$$\begin{aligned} &K_{11}=\hat{E}(1-2\nu)\left(\frac{1}{r_i^2}-\frac{1}{r_o^2}\right) \quad \text{and} \quad K_{12}=\hat{E}_b(1-2\nu_b)\left(\frac{1}{r_o^2}-\frac{1}{r_{o,b}^2}\right), \\ &K_{21}=\hat{E}A_s\left(\frac{2\nu(1-2\nu)}{r_i^2}-c_L\frac{r_i^2+r_o^2(1-2\nu)}{r_i^2r_o^2}\right), \\ &K_{22}=\hat{E}A_s\left(\frac{\hat{E}_bA_{s,b}}{\hat{E}A_s}\frac{2\nu_b(1-2\nu_b)}{r_{o,b}^2}+c_L\frac{r_{o,b}^2+r_o^2(1-2\nu_b)}{r_{o,b}^2r_o^2}\right), \\ &R_1=p_i-p_e \quad \text{and} \quad R_2=N+2\nu p_iA_s+2\nu_bp_eA_{s,b}-c_L\hat{E}A_s\left(\frac{p_i}{\hat{E}}-\frac{p_e}{\hat{E}_b}\right), \\ &c_L=\frac{EA_s+E_bA_{s,b}+KL}{\hat{E}A_s(\nu_b-\nu)}. \end{aligned} \quad \textbf{(47)}$$

The solution presented in Eq. (46) has a factor $(\nu_b - \nu)$ in the denominators of C_z and c_L. This factor results in numerical problems if $\nu_b = \nu$, and hence, for this particular case, a fictitious small perturbation of either ν or ν_b may be introduced to avoid singularities in the numerical computation of the solution.

Alternatively, the issue with the $(\nu_b - \nu)$ factor may be circumvented by solving the equations in a different manner, more specifically by solving for different undetermined coefficients first. The alternative, albeit more involved, solution is given by

$$C_{r1,b}=\frac{K_{22}R_1-K_{12}R_2}{K_{11}K_{22}-K_{12}K_{21}}\quad\text{and}\quad C_{r2,b}=\frac{-K_{21}R_1+K_{11}R_2}{K_{11}K_{22}-K_{12}K_{21}},$$

$$C_{r1}=\left(1+\frac{1-2\nu_b}{r_{o,b}^2}r_o^2c_A\right)C_{r1,b}+r_o^2(1+c_B)C_{r2,b}-r_o^2c_A\frac{p_e}{\hat{E}_b}-r_o^2\frac{N}{2\nu\hat{E}A_s},$$

$$C_{r2}=-\frac{1-2\nu_b}{r_{o,b}^2}c_AC_{r1,b}-c_BC_{r2,b}+c_A\frac{p_e}{\hat{E}_b}+\frac{N}{2\nu\hat{E}A_s}, \qquad \textbf{(48)}$$

$$C_z=\frac{L}{\nu_b}\left(\frac{1-2\nu_b}{r_{o,b}^2}C_{r1,b}-C_{r2,b}-\frac{p_e}{\hat{E}_b}\right),$$

where

$$K_{11}=\alpha(r_o)-\frac{\hat{E}_b(1-2\nu_b)}{r_{o,b}^2}\left(1-\frac{r_{o,b}^2}{r_o^2}\right)\quad\text{and}\quad K_{12}=\beta(r_o),$$

$$K_{21}=\alpha(r_i)\quad\text{and}\quad K_{22}=\beta(r_i),$$

$$R_1=-\left(1+\frac{\hat{E}}{\hat{E}_b}\gamma(r_o)\right)p_e-\frac{\gamma(r_o)+(\nu/\nu_b)}{c_A}\frac{N}{2\nu A_s},$$

$$R_2=-\frac{\hat{E}}{\hat{E}_b}\gamma(r_i)p_e-p_i-\frac{\gamma(r_i)+(\nu/\nu_b)}{c_A}\frac{N}{2\nu A_s}, \qquad \textbf{(49)}$$

$$c_A=\frac{\hat{E}A_s(1-\nu)+\hat{E}_bA_{s,b}(1-\nu_b)+KL}{2\nu\nu_b\hat{E}A_s}\quad\text{and}\quad c_B=\frac{\nu_b\hat{E}_bA_{s,b}}{\nu\hat{E}A_s}-c_A,$$

$$\alpha(r)=-\frac{\hat{E}(1-2\nu)}{r^2}\left(1+\frac{1-2\nu_b}{1-2\nu}\frac{r^2}{r_{o,b}^2}\gamma(r)\right)\quad\text{and}\quad\gamma(r)=\left(1+(1-2\nu)\frac{r_o^2}{r^2}\right)c_A-\frac{\nu}{\nu_b},$$

$$\beta(r)=-\hat{E}(1-2\nu)\frac{r_o^2}{r^2}(1+c_B)-\hat{E}\left(\frac{\nu}{\nu_b}+c_B\right).$$

5.3 Heated Two-Layer Cylinder under Plane Strain Conditions

In this section, the boundary condition shown in Figure 3 a) will be solved for a cylinder subjected to heat, but no other loading. The temperature expansion coefficients of the inner and outer cylinder layers are generally assumed to be different. Consequently, if the cylinder is subjected to a uniform change in temperature ΔT, the contact pressure between the surfaces will change. The applied temperature is to be uniform over the whole volume of the two-layer cylinder.

Eq. (33) contains the stress fields for the inner and outer cylinder layers. The axial displacement field coefficients C_z and $C_{z,b}$ are still zero, as given by Eq. (36), since the cylinder is fully fixed axially. Consequently, four equations must be established in order to explicitly determine the remaining four displacement field coefficients. Two equations are

obtained from the boundary conditions at the inner radius of the inner cylinder and at the outer radius of the outer cylinder. The boundary conditions are given by Eq. (37), which now simplifies to

$$\sigma_{rr}(r_i)=\sigma_{rr,b}(r_{o,b})=0\,, \tag{50}$$

since internal and external pressures are not considered in the present load case.

The two final equations are established from the continuity of radial displacements and radial stresses at the interface between the cylinder layers, Eqs. (38) and (39). From Eqs. (33), (38), (39) and (50), the following system of equations may then be formulated:

$$\begin{bmatrix} -\frac{\hat{E}(1-2\nu)}{r_o^2} & \hat{E} & \frac{\hat{E}_b(1-2\nu_b)}{r_o^2} & -\hat{E}_b \\ \frac{1}{r_o} & r_o & -\frac{1}{r_o} & -r_o \\ -\frac{(1-2\nu)}{r_i^2} & 1 & 0 & 0 \\ 0 & 0 & -\frac{(1-2\nu_b)}{r_{o,b}^2} & 1 \end{bmatrix} \begin{bmatrix} C_{r1} \\ C_{r2} \\ C_{r1,b} \\ C_{r2,b} \end{bmatrix} = \begin{bmatrix} \Delta T\left(\hat{E}\alpha(1+\nu)-\hat{E}_b\alpha_b(1+\nu_b)\right) \\ 0 \\ \alpha\Delta T(1+\nu) \\ \alpha_b\Delta T(1+\nu_b) \end{bmatrix} \tag{51}$$

Solving the system of equations yields the following expressions for the coefficients:

$$\begin{bmatrix} C_{r1} \\ C_{r2} \\ C_{r1,b} \\ C_{r2,b} \end{bmatrix} = \begin{bmatrix} \frac{A_o\Delta T(\alpha_b(1+\nu_b)-\alpha(1+\nu))\hat{E}_b A_{s,b}(1-2\nu_b)r_i^2}{\hat{E}A_s(1-2\nu)\left(A_{o,b}+A_o(1-2\nu_b)\right)+\hat{E}_b A_{s,b}(1-2\nu_b)\left(A_i+A_o(1-2\nu)\right)} \\ C_{r1}\frac{1-2\nu}{r_i^2}+\alpha\Delta T(1+\nu) \\ -\frac{A_o\Delta T(\alpha_b(1+\nu_b)-\alpha(1+\nu))\hat{E}A_s(1-2\nu)r_{o,b}^2}{\hat{E}A_s(1-2\nu)\left(A_{o,b}+A_o(1-2\nu_b)\right)+\hat{E}_b A_{s,b}(1-2\nu_b)\left(A_i+A_o(1-2\nu)\right)} \\ C_{r1,b}\frac{1-2\nu_b}{r_{o,b}^2}+\alpha_b\Delta T(1+\nu_b) \end{bmatrix} \tag{52}$$

5.4 Heated and Axially Loaded Two-Layer Cylinder under Generalized Plane Strain Conditions

Similar to the derivation of the heating solution for a two-layer cylinder with fixed axial supports, a derivation will be made for a heated two-layer cylinder mounted on axial spring support, as shown in Figure 3 b).

As in the previous cases, Eq. (33) contains the stress fields for the inner and outer cylinder layers. The stress fields contain six undetermined coefficients, and consequently, six equations must be established in order to explicitly determine the fields. The radial boundary

conditions given by Eq. (50) provide two relations. In addition, the continuity requirements at the interface between the layers, Eq. (38) and Eq. (39), still apply. Furthermore, since generalized plane strain is required, the axial displacement field coefficients in the two layers must be equal, in accordance with Eq. (43). Finally, the last equation can be established by considering the force balance in axial direction between the cylinder layers and the axial spring force:

$$\sigma_{zz}A_s + \sigma_{zz,b}A_{s,b} = -Ku_z(L) = -KC_z \,. \tag{53}$$

Note, with regard to Eq. (53), that the axial load *N*, as displayed for the relevant boundary condition in Figure 3 b), has intentionally been omitted. The axial load *N* was included when calculating the solution for a two-layer cylinder subjected to pressure in Section 5.2. That solution will later be superposed to the solution derived in the current section.

By combining Eqs. (33), (38), (39), (43), (50) and (53) the final system of five equations in five unknowns can be established and expressed by

$$\begin{bmatrix} -\frac{\hat{E}(1-2\nu)}{r_o^2} & \hat{E} & \frac{\hat{E}\nu - \hat{E}_b\nu_b}{L} & \frac{\hat{E}_b(1-2\nu_b)}{r_o^2} & -\hat{E}_b \\ \frac{1}{r_o} & r_o & 0 & -\frac{1}{r_o} & -r_o \\ -\frac{(1-2\nu)}{r_i^2} & 1 & \frac{\nu}{L} & 0 & 0 \\ 0 & 0 & \frac{\nu_b}{L} & -\frac{(1-2\nu_b)}{r_{o,b}^2} & 1 \\ 0 & 2\nu\hat{E}A_s & \frac{\hat{E}A_s(1-\nu)+\hat{E}_bA_{s,b}(1-\nu_b)}{L}+K & 0 & 2\nu_b\hat{E}_bA_{s,b} \end{bmatrix} \begin{bmatrix} C_{r1} \\ C_{r2} \\ C_z \\ C_{r1,b} \\ C_{r2,b} \end{bmatrix} = \begin{bmatrix} \Delta T\left(\hat{E}\alpha(1+\nu)-\hat{E}_b\alpha_b(1+\nu_b)\right) \\ 0 \\ \alpha\Delta T(1+\nu) \\ \alpha_b\Delta T(1+\nu_b) \\ \Delta T\left(\hat{E}A_s\alpha(1+\nu)+\hat{E}_bA_{s,b}\alpha_b(1+\nu_b)\right) \end{bmatrix}. \tag{54}$$

The solution of this system of equations may be written on the following form:

$$\begin{aligned} C_{r1,b} &= \frac{R_1K_{22}-R_2K_{12}}{K_{11}K_{22}-K_{12}K_{21}} \quad \text{and} \quad C_{r2,b} = \frac{-R_1K_{21}+R_2K_{11}}{K_{11}K_{22}-K_{12}K_{21}}\,, \\ C_{r2} &= \frac{\Delta T}{2\nu}\left(\alpha(1+\nu)-c_B\alpha_b(1+\nu_b)\right) - \frac{c_A(1-2\nu_b)}{2\nu r_{o.b}^2}C_{r1,b} - \frac{2\nu_b\left(\hat{E}_bA_{s,b}/\hat{E}A_s\right)-c_A}{2\nu}C_{r2,b}\,, \\ C_z &= \frac{L}{\nu_b}\alpha_b\Delta T(1+\nu_b) + \frac{L(1-2\nu_b)}{\nu_b r_{o.b}^2}C_{r1,b} - \frac{L}{\nu_b}C_{r2,b}\,, \\ C_{r1} &= -r_o^2C_{r2} + C_{r1,b} + r_o^2C_{r2,b}\,, \end{aligned} \tag{55}$$

where

$$K_{11} = \frac{\hat{E}_b(1-2\nu_b) - \hat{E}(1-2\nu)}{r_o^2} + (1-2\nu_b)\frac{\hat{E}\nu - \hat{E}_b\nu_b}{\nu_b r_{o,b}^2} - \frac{\hat{E}c_A(1-\nu)(1-2\nu_b)}{\nu r_{o,b}^2},$$

$$K_{12} = -\hat{E}\left(1-2\nu+\frac{\nu}{\nu_b}\right) - \frac{\left(2\nu_b\hat{E}_b A_{s,b} - \hat{E}A_s c_A\right)(1-\nu)}{\nu A_s},$$

$$K_{21} = \frac{\nu(1-2\nu_b)}{\nu_b r_{o,b}^2} - \frac{1-2\nu}{r_i^2} - \left(1+(1-2\nu)\frac{A_o}{A_i}\right)\frac{c_A(1-2\nu_b)}{2\nu r_{o,b}^2},$$

$$K_{22} = -(1-2\nu)\frac{A_o}{A_i} - \frac{\nu}{\nu_b} - \left(1+(1-2\nu)\frac{A_o}{A_i}\right)\frac{2\nu_b\left(\hat{E}_b A_{s,b}/\hat{E}A_s\right) - c_A}{2\nu},$$

$$R_1 = \Delta T\left(\hat{E}\alpha(1+\nu) - \frac{\hat{E}\nu\alpha_b(1+\nu_b)}{\nu_b} - \frac{\hat{E}(1-\nu)}{\nu}\left(\alpha(1+\nu) - c_B\alpha_b(1+\nu_b)\right)\right), \quad \textbf{(56)}$$

$$R_2 = \Delta T\left(\alpha(1+\nu) - \frac{\nu}{\nu_b}\alpha_b(1+\nu_b) - \left(1+(1-2\nu)\frac{A_o}{A_i}\right)\frac{\left(\alpha(1+\nu) - c_B\alpha_b(1+\nu_b)\right)}{2\nu}\right),$$

$$c_A = \frac{\hat{E}A_s(1-\nu) + \hat{E}_b A_{s,b}(1-\nu_b) + KL}{\nu_b\hat{E}A_s}$$

and $$c_B = \frac{\hat{E}A_s(1-\nu) + \hat{E}_b A_{s,b}(1-2\nu_b) + KL}{\nu_b\hat{E}A_s}.$$

5.5 Combined Pressure and Thermal Loading

The materials in each cylinder layer have been assumed to be linearly elastic, homogenous and isotropic, and deformations have been assumed small in this study. Consequently, the principle of superposition is valid. The displacement fields for the boundary conditions found in Figure 3 for combined pressure and temperature loading, may therefore be calculated by simple addition of the individual fields corresponding to each load case. Thus, under combined pressure and temperature loading, the displacement field for the axially fixed configuration (Figure 3 a) can be found by adding the displacement field coefficients in Eqs. (41) and (52), and the displacement field for the spring mounted and axially free systems (Figure 3 b) can be determined by adding the field coefficients in Eqs. (48) and (55).

6 VALIDATION OF THE TWO-LAYER SOLUTIONS

6.1 Verification Cases

Two cases are studied for the purpose of verification. The material data and loading conditions for the cases are given in Table 1.

Table 1 – Material and loading parameters for two verification cases

Input parameter	Symbol	Unit	Configuration 1	Configuration 2
Inner radius	r_i	m	0.200	0.060
Outer radius of inner layer	r_o	m	0.250	0.070
Outer radius	$r_{o,b}$	m	0.350	0.080
Young's modulus of inner layer	E	GPa	191	16
Poisson's ratio of inner layer	v	-	0.29	0.44
Coeff. of thermal exp., inner layer	α	$(°C)^{-1}$	$1.7 \cdot 10^{-5}$	$2.9 \cdot 10^{-5}$
Young's modulus of outer layer	E_b	GPa	200	200
Poisson's ratio of outer layer	v_b	-	0.30	0.30
Coeff. of thermal exp., outer layer	α_b	$(°C)^{-1}$	$1.2 \cdot 10^{-5}$	$1.2 \cdot 10^{-5}$
Change in temperature	ΔT	°C	100	85
Internal pressure	p_i	MPa	20	15
External pressure	p_e	MPa	5	0

Configuration 1 exemplifies a two-layered cylinder consisting of a combination of two thick-walled cylinder layers made from typical steels. The inner layer has typical corrosion resistant steel alloy (CRA) properties and the outer layer has typical Carbon-Manganese (CMn) graded steel properties. Configuration 2 exemplifies a two-layered cylinder consisting of an outer CMn steel layer lined with a thick inner lead layer. This combination was chosen due to the significant differences in material properties and thermal expansion coefficients between the two layers. The first configuration is not a physically relevant example, whereas the second may be more realistic in engineering contexts. Neither configuration was chosen, however, to demonstrate physical behavior. Both configurations are meant to be suitable in analyses aimed at verifying that the analytical equations developed in Section 5 are exact. For that purpose, cylinders with extremely thick walls were chosen. Examples of more realistic engineering applications are discussed in Section 7, where lined and clad offshore pipelines are investigated.

6.2 Finite Element Analyses

6.2.1 Element Type and Boundary Conditions

Finite element (FE) analyses have been conducted using the commercially available software program Abaqus [2012]. The 8-node brick element C3D8R was used. This is a bi-linear solid element with reduced integration and hourglass control.

The Abaqus models were established with boundary conditions as illustrated on the two cylinder segments in Figure 3 a) and b). In Figure 3 b), the dashed lines indicate a kinematic coupling between a reference point (RP) and the cylinder end surface. In the FE model, the reference point was taken as a master node, and the cylinder end surface was taken as a slave surface. For the case of non-zero axial spring stiffness K and applied axial force N, both the spring force and the axial force were applied at the reference point (RP), as indicated in Figure 3 b).

It has been assumed that cross-sections plane and perpendicular to the cylinder axis remain plane and perpendicular after deformation. Thus, there are no shear forces acting due to friction or axial fixation between the layers. It is therefore inconsequential how the bond between the layers is modeled. As mentioned above, the reference point shown in Figure 3 b) creates a master-slave relation, where the cylinder end surface is a slave surface. Consequently, all nodes on this surface are slave nodes. In order to model contact between the two layers in the cylinders, one of the surfaces would have to be a slave and the other a master surface at the interface between the layers. Thus, at the end surface, the interface between the layers would contain two sets of master-slave relations, which is not possible to solve for in Abaqus. To avoid problems with master-slave relations along the circumferential line at the interface between layers, the interaction between the layers was therefore not modeled as a contact surface. Instead, the two-layer cylinder was modeled as a single cylinder with varying material properties through the thickness.

6.2.2 Geometry

The cylinders described in Figure 3 are loaded with internal pressure, external pressure, uniform temperature and potentially a uniformly distributed axial loading over the end cross-section. This represents an axisymmetric problem, since the only variation in stresses is a function of the radial coordinate. This implies, theoretically, that it is not necessary to model the full cylinder. Thus, it would suffice to model a small slice with a certain limited angle φ as shown in Figure 7. Both such a limited axisymmetric model and a

full circular model have been considered in the present study. Their respective strengths and drawbacks are briefly discussed below.

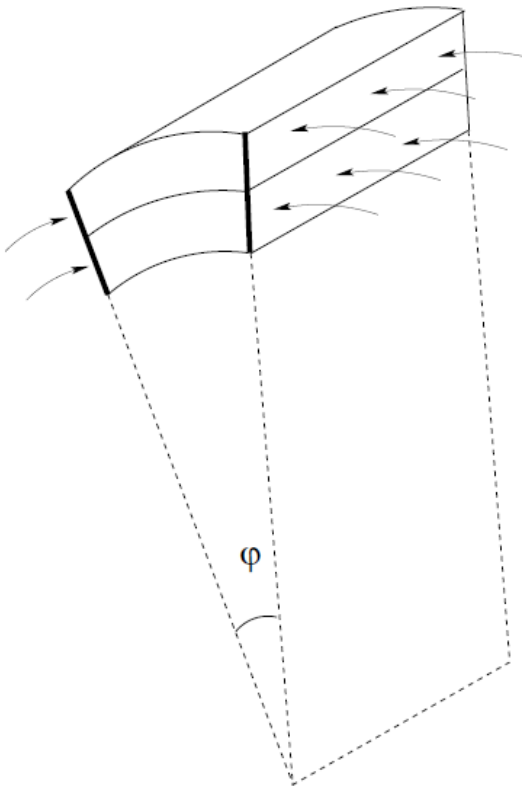

Figure 7 – Model of axisymmetric two-layer cylinder. (Boldfaced lines indicate where boundary conditions are particularly challenging).

The reason for choosing an axisymmetric model (i.e., modeling only a slice of the cylinder) is simply a practical one; it normally allows a much smaller model in terms of the number of elements. The enforcement of appropriate boundary conditions may cause some problems, however. As mentioned (Section 6.2.1), the boundary conditions are enforced at the reference point (center of cylinder) through a master-slave relation between the reference point ("the master") and the elements along the circumference ("the slaves"). Therefore, at the radial boundary lines (defining the outer boundaries of the "slice"), which are indicated by thick lines in Figure 7, other boundary conditions than those enforced by the master cannot be obtained. Hence, the symmetry boundary conditions cannot be satisfied along these lines. Effects of this lack of symmetry have been investigated using a very long axisymmetric model for verification case 2. Axial stress results are shown in Figure 8. Near the radial (slice) boundary lines, axial stresses can be seen to vary significantly, and to be particularly high near the layer interface. Further away from the radial boundary lines, there are no similar variations. In axisymmetric problems one would expect equal results along the

circumferential axis. As this is not the case, the axial stress fluctuations must be caused by the mentioned lack of symmetry along the radial ("slice") boundary lines, and not caused by any possible interaction between the layers.

At some distance away from the cylinder end, stress results seem to be stationary. Thus, by choosing a sufficiently long axisymmetric slice model, a section at some significant distant from the cylinder end could be used for verification purposes. Such results would be only marginally less accurate than results from full cylinder analyses. However, as the purpose of the verification in this section is to document that the developed theory is exact, even small variations in expected results are not considered acceptable. Therefore, a model of the full circular cylinder geometry was chosen for the final verification calculations. Since results from a full circular model are independent of length, a shorter model compared to the one used in the axisymmetric analysis may be chosen. As a consequence, the total numbers of elements in the two types of models are of similar magnitudes.

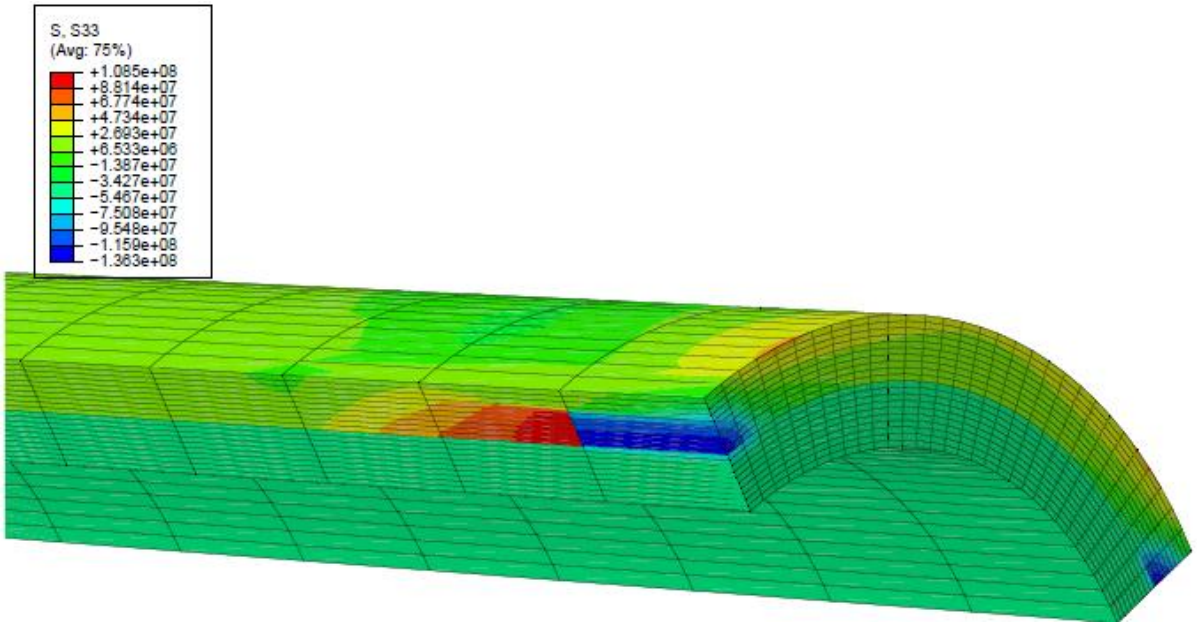

Figure 8 – Axial stresses near the end boundary for verification case 2, with axisymmetric model and axially free end.

The geometry of the full circular model for verification case 2 is as illustrated in Figure 3. The length is taken equal to 10% of the outer diameter. Mesh division is discussed below. Computed axial stresses, for the same loading and boundary condition case considered in the axisymmetric analysis, are shown in Figure 9. These are comparable to the axisymmetric results in Figure 8, but shows, unlike those in Figure 8, no fluctuations caused by possible boundary condition issues and possible interaction between layers. Manual

inspection of each individual element shows that there is no variation in axial stress within each layer as a function of the radial or axial coordinates. These results confirm the validity of the displacement assumption in Eq. (25).

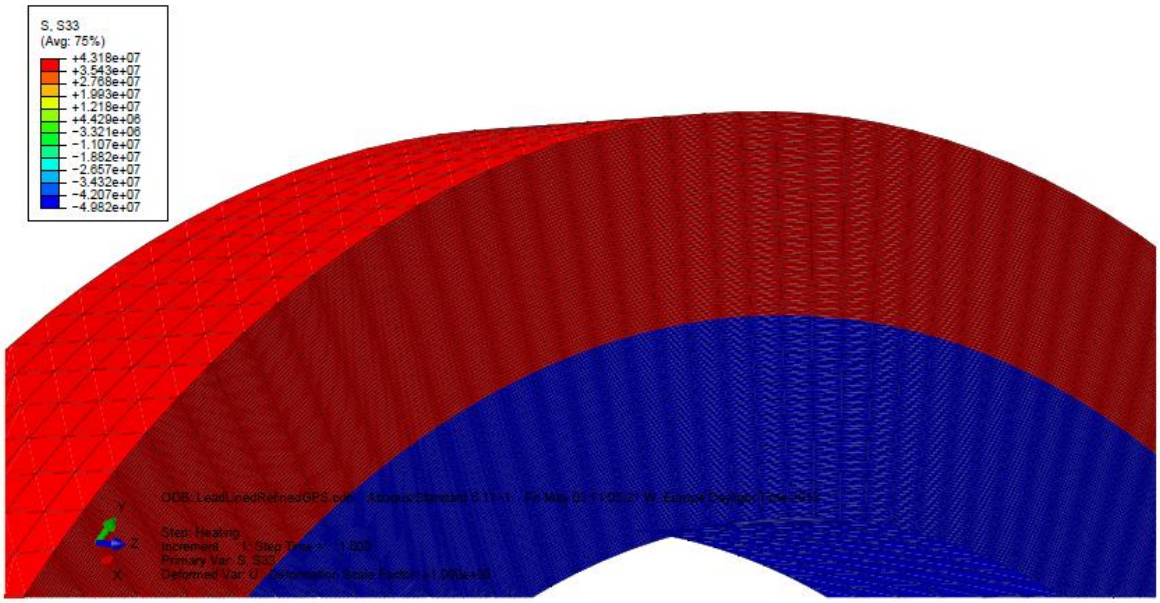

Figure 9 – Axial stresses in the full cylinder model for verification case 2 and an axially free boundary.

6.2.3 Mesh Refinement and Convergence

A convergence study was performed of the finite element solution for increasing mesh refinement. Convergence to 5 significant digits was assumed complete. Full convergence was achieved globally, but the local radial stresses at the interface between cylinder layers did not converge. Only 1 element in the axial direction is necessary for convergence of axial stresses, but 6 elements were chosen in the axial direction to ensure a good aspect ratio. In the hoop direction, convergence was achieved with 180 elements. In the radial direction, overall convergence was achieved with approximately 20 elements over the thickness for both configurations 1 and 2. However, at the interface between the layers, at r_i and at $r_{o,b}$, full convergence was not achieved even with 120 elements over the thickness. A small discontinuity of the radial stresses occurred at the interface, and a slight difference between applied pressure and radial stress was observed at the inner radius r_i and outer radius $r_{o,b}$ for all cases considered. In Figure 10, the radial stresses for configuration 1, with an axially free boundary, are shown as an example. In Figure 10 a), the radial stresses appear continuous over the interface, but when zooming in on the curve near the interface between the layers, at

r = 0.25, a clear discontinuity is observed. This discontinuity was approximately three times larger in magnitude for 20 elements than for 120 elements over the thickness.

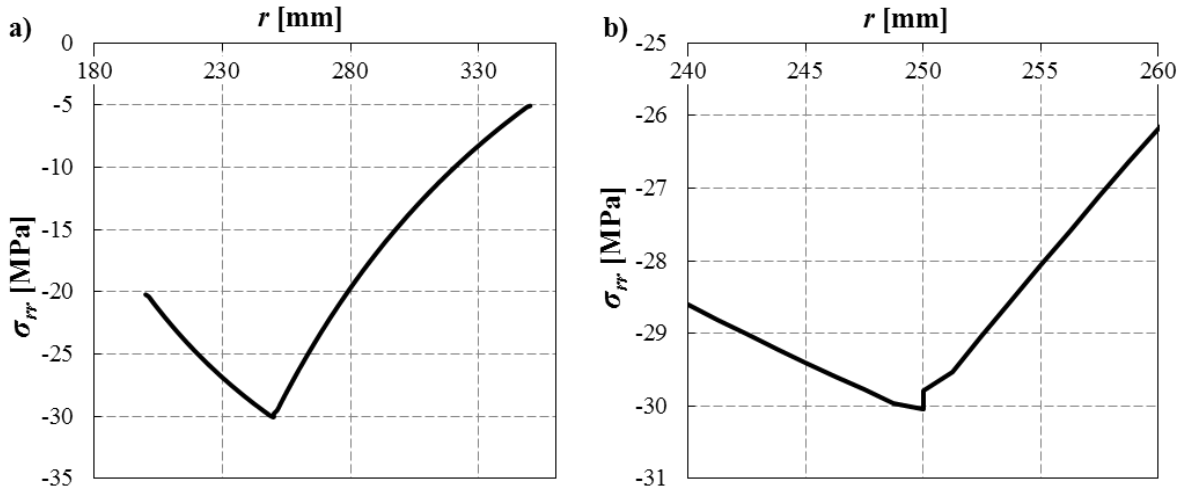

Figure 10 - Radial stresses for configuration: a) overall distribution, b) detail of local variation near the interface between layers.

The number of elements in the full cylinder analyses included a total of 129600 solid elements, corresponding to approximately 500000 degrees of freedom. The discontinuity at the interface between layers declines with increasing number of elements, but further refinement was considered unnecessary since the discontinuity is obviously unphysical (the contact pressure cannot be different on the two surfaces). Consequently, 129600 elements were used in all the verification cases, and discontinuities between layers were disregarded as unphysical. Since the radial stress at the interface between layers is discontinuous in the FE solutions, almost regardless of element mesh refinement, it is rather inefficient to determine interface stresses by means of FE analyses. One solution to the convergence issues along the radial coordinate would be to treat the problem according to the axisymmetric approach shown in Figure 7, thereby reducing the number of elements dramatically while still allowing for more elements in radial direction. However, as discussed in Section 6.2.2, this approach introduces other issues which leads to problems with the axial stresses and is therefore not an ideal solution either.

6.3 Comparisons between Finite Element Results and the Analytical Solutions

As described in Section 6.1, the verification study was performed using two different two-layer cylinder configurations, with geometric properties, material properties and applied

loading as specified in Table 1. The two boundary conditions illustrated in Figure 3, i.e., axially fixed and axially free, were considered for both of the configurations. In addition, an analysis was performed (on configuration 2), with spring stiffness K = 10 GN/m and axial force N = -450.5 kN on a cylinder segment of length L = 0.015 m. The values of K and N were selected such that the axial displacement of the end surface was reduced by a factor of two when compared to the results for the axially free boundary condition.

The variation in radial stress over the combined wall thickness, calculated both analytically with the derived, explicit stress expressions and by means of FE analysis, is shown in Figure 11 for the case with non-zero K and N and combined pressure and temperature loading.

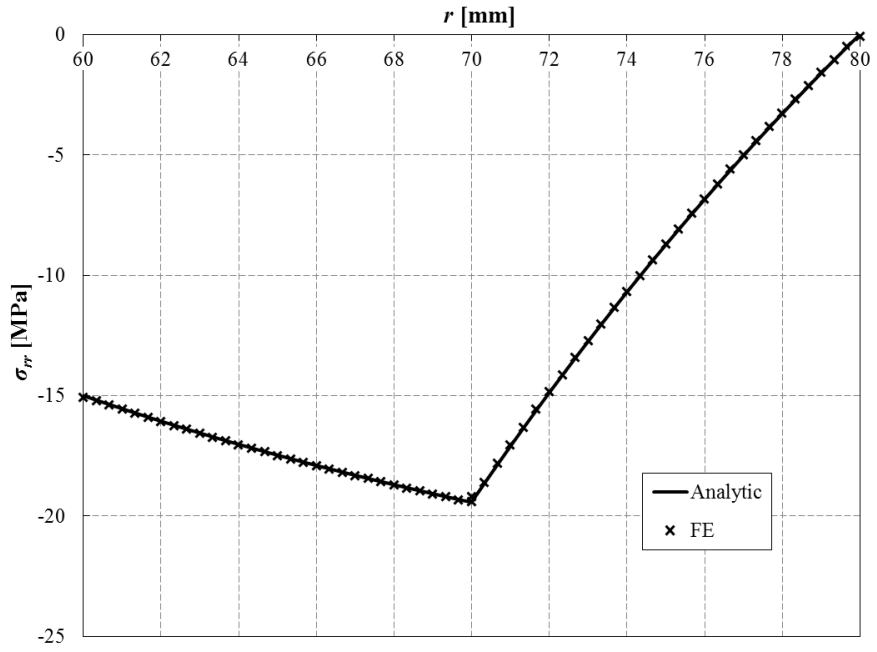

Figure 11 – Radial stress versus radial coordinate for configuration 2 with the spring-mounted boundary condition; K = 10 GN/m and N = -450.5 kN.

In Figure 11 we see that the radial stress balances the applied internal pressure of 15 MPa at the inner surface $r = r_i$ (= 60 mm) and goes to zero at the outer surface $r = r_{o,b}$ (= 80 mm) since no external pressure is applied. The contact pressure between the lead liner (inner layer) and the backing steel (outer layer) is 19.4 MPa. Most importantly, Figure 11 shows that the results based on the analytical formulae derived in this study are virtually identical to the FE results (except for a small deviation at the interface between the layers, where the FE results are slightly inaccurate as described in Section 6.2.3).

For the same verification case, the analytical hoop stress calculations are compared to FE results in Figure 12.

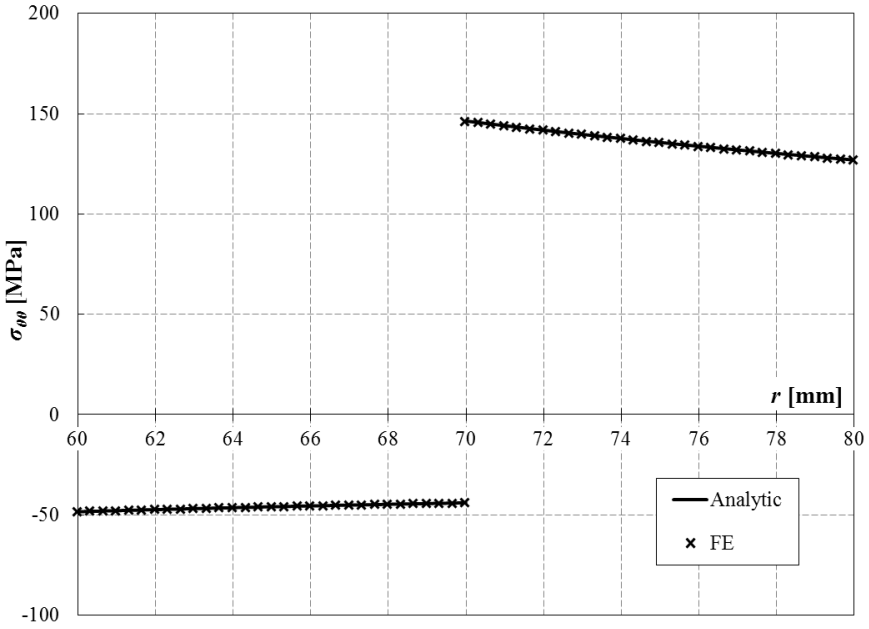

Figure 12 – Hoop stress versus the radial coordinate for configuration 2 with the spring-mounted boundary condition; K = 10 GN/m and N = -450.5 kN.

From Figure 12 it is clear that the lead liner has a compressive hoop stress (negative), while the backing steel is in tension (positive). This is not surprising, since the thermal expansion coefficient of the lead liner is more than a factor of two larger than the expansion coefficient of the backing steel (Table 1). Again it may be observed that the analytical results are indistinguishable from the FE results. In fact, the same excellent correspondence between analytical and FE-derived results was demonstrated for both radial and hoop stresses in all the five verification analyses. For this reason, the results of the remaining analyses are not shown in this section. However, a complete presentation of the results is included in Appendix B.

It should be emphasized that the analytical radial and hoop stress calculations plotted in Figure 11 and Figure 12 are the sum of stresses due to pure pressure loading and pure thermal loading. Consequently, it is evident from the figures that the application of the principle of superposition gives excellent accuracy for the relevant verification case, thereby justifying the strategy of handling the individual load types separately, as noted in Section 5.5. The figures shown in Appendix B display the individual stresses due to pure pressure loading and pure thermal loading, as well as the stresses from the combined effect of temperature and pressure.

The axial stresses in the two cylinder layers for the five verification cases are compared in Table 2. As seen from columns 3 and 5 in the table, there is virtually no difference between the analytically and numerically (FEA) calculated values. Therefore, only the analytically predicted values are presented in the table for each layer and load case. As noted in Section 04, the axial stress is constant, i.e., independent of the radial coordinate *r*, in each layer of the cross-section.

Table 2 – Axial stresses in the cylinder layers for the two configurations and three axial boundary conditions, and comparison of stresses calculated analytically (σ_{zz}^{AN}) and by means of FE analyses (σ_{zz}^{FE}).

Load case	σ_{zz} [Pa]	$\left\|1-\frac{\sigma_{zz}^{AN}}{\sigma_{zz}^{FE}}\right\|$	$\sigma_{zz,b}$ [Pa]	$\left\|1-\frac{\sigma_{zz,b}^{AN}}{\sigma_{zz,b}^{FE}}\right\|$
Configuration 1, fully restrained axially				
Temperature	$-3.53\cdot10^{8}$	$2.15\cdot10^{-6}$	$-2.29\cdot10^{8}$	$7.63\cdot10^{-7}$
Pressure	$1.13\cdot10^{6}$	$3.77\cdot10^{-4}$	$1.44\cdot10^{6}$	$1.08\cdot10^{-5}$
Temperature and pressure	$-3.52\cdot10^{8}$	$9.43\cdot10^{-7}$	$-2.28\cdot10^{8}$	$8.36\cdot10^{-7}$
Configuration 1, axially free				
Temperature	$-9.96\cdot10^{7}$	$3.53\cdot10^{-7}$	$3.74\cdot10^{7}$	$1.78\cdot10^{-6}$
Pressure	$-1.74\cdot10^{5}$	$1.18\cdot10^{-6}$	$6.51\cdot10^{4}$	$4.68\cdot10^{-5}$
Temperature and pressure	$-9.98\cdot10^{7}$	$3.54\cdot10^{-7}$	$3.74\cdot10^{7}$	$1.69\cdot10^{-6}$
Configuration 2, fully restrained axially				
Temperature	$-6.21\cdot10^{7}$	$1.65\cdot10^{-7}$	$-1.91\cdot10^{8}$	$6.04\cdot10^{-7}$
Pressure	$-6.03\cdot10^{6}$	$6.10\cdot10^{-6}$	$2.52\cdot10^{7}$	$3.65\cdot10^{-6}$
Temperature and pressure	$-6.81\cdot10^{7}$	$3.89\cdot10^{-7}$	$-1.65\cdot10^{8}$	$1.25\cdot10^{-6}$
Configuration 2, axially free				
Temperature	$-4.22\cdot10^{7}$	$8.94\cdot10^{-7}$	$3.66\cdot10^{7}$	$3.12\cdot10^{-6}$
Pressure	$-7.65\cdot10^{6}$	$6.65\cdot10^{-6}$	$6.63\cdot10^{6}$	$2.05\cdot10^{-5}$
Temperature and pressure	$-4.98\cdot10^{7}$	$2.64\cdot10^{-7}$	$4.32\cdot10^{7}$	$5.08\cdot10^{-7}$
Configuration 2, spring-mounted, K = 10 GN/m and N = -450.5 kN				
Temperature	$-4.47\cdot10^{7}$	$9.90\cdot10^{-6}$	$7.17\cdot10^{6}$	$7.90\cdot10^{-4}$
Pressure	$-1.42\cdot10^{7}$	$8.10\cdot10^{-5}$	$-6.83\cdot10^{7}$	$1.88\cdot10^{-4}$
Temperature and pressure	$-5.90\cdot10^{7}$	$2.70\cdot10^{-5}$	$-6.12\cdot10^{7}$	$3.02\cdot10^{-4}$

From the results presented in Table 2, it is observed that the maximum relative difference between the analytical results and the FE results is approximately 0.08 %. This

completely negligible deviation occurs for pure thermal loading in the spring-mounted condition with non-zero spring stiffness and axial load. The analytical expressions derived in Section 5 are exact when the assumptions listed in Section 2.1 are justified. Hence, the excellent agreement with FE results was expected. The fact that the results are in nearly perfect correspondence across the range of cylinder configurations, load cases and boundary conditions examined in the present verification study, clearly demonstrates that the analytical expressions have been derived correctly.

7 APPLICATION – LINED AND CLAD PIPELINES

7.1 Current Design Practice – Failure Modes

The new understanding of stresses and stress distributions in heated and pressurized lined and clad pipelines derived herein may have implications for pipeline design concepts. In the following, a selection of failure modes will be examined based on stress calculations with the new analytical expressions. These failure modes comprise:

- Burst (Rupture of the pipe wall due to internal over pressure)
- Collapse (Local buckling of the pipe wall due to external over pressure)
- Combined loading (Local buckling of the pipe due to axial force, bending and pressure)
- Fatigue cracking in girth welds due to cyclic loading

The failure modes mentioned in the list above are treated in the world leading offshore standard for pipelines DNV-OS-F101 [2012], and the American standard API RP 1111 [2009]. How the specific design equations are formulated in the two codes rely on for instance mill test data, fabrication processes and production tolerances. Hence the equations themselves are not particularly physically intuitive and their exact formulation would require significant explanation if included in the present context. There are, however, three simple and important observations to be made, which will influence the following discussion.

1. Pressures are accounted for by membrane hoop stresses, using equations similar to the formulation in Eq. (7), i.e. constant stresses are assumed through the pipe wall thickness.
2. Axial stresses directly influence the combined loading and fatigue cracking criteria.
3. All listed design criteria, with exception of fatigue cracking, are functions of the yield stress.

Apart from the three observations listed above, the exact formulation of the design equations will not be discussed further. The interested reader may find complete formulations and references to the background material in the design codes themselves [DNV-OS-F101, 2012; API RP 1111, 2009].

7.2 Potential Problems with Current Design Practice

Presently, the design practice according to DNV-OS-F101 [2012] and API RP 1111 [2009] for lined and clad pipelines is based on the principle that the liner or cladding is treated only as a corrosion inhibitor and not as a structural load carrying member. In other words, the corrosion resistance properties of the inner cylinder layer are relied on for the proper functioning of the pipe, but its structural function is disregarded. As a result, the added strength it provides to the combined cross-section due to the extra steel material is not utilized in design. This is in itself assumed to be a conservative approach. However, by disregarding its structural function, the stresses inflicted by the liner or clad layer on the combined cross-section are also left unaccounted for. These are due to the different material characteristics of the inner liner (or cladding) and the outer backing steel; that is, the generally higher temperature expansion coefficient and the marginally lower Young's modulus and Poisson's ratio of the liner (or cladding) than of the CMn backing steel layer. When heating and pressurizing a lined pipe, such differences in material characteristics will result in increased contact pressure between the layers, which in turn will alter the distributions of radial and hoop stresses in both layers as compared to those obtained for a monolithic cross-section.

The following discussions aim to show that the liner has relevant impact on the stresses in the backing steel, which are not necessarily conservatively assessed in all loading conditions when applying the current practice of disregarding the contribution to structural strength from liner or cladding layers. Furthermore, potential consequences and impacts on relevant failure modes, as listed in Section 7.1, will be indicated, albeit not discussed in detail, for both the backing steel and the liner or cladding itself. The investigation is based on two selected and representative case studies. As observed in Section 7.1, all failure modes are dependent on the stresses and the yield stress (with the exception of fatigue cracking which only depends on the stresses). In order to simplify the discussion, and to avoid entering lengthy and detailed discussions on the specific formulation for each individual design equation, comparisons will be based directly on stresses and von Mises stresses estimated for the cases of 1) including the structural properties of the liner and 2) disregarding the liner as a load-carrying member.

7.3 Assumptions and Limitations

As will be demonstrated in the following, CRA liners or cladding are often expected to undergo plastic deformation under normal design conditions. The theory developed in this report only covers elastic deformation and can therefore not give precise estimations for response in the plastic range. Effects of assuming linear elasticity will be discussed in each relevant context. The initial stress state in the liner or cladding due to the production process [Vedeld et al. 2012b] and due to plastic deformation cycles during installation [Focke, 2007, Hilberink et al. 2011] will further complicate the issue of the plastic strain history. The cases studied herein are meant to illustrate issues which are currently unaccounted for in industry practice, but not necessarily to provide solutions to them. Consequently, for clarity of argument and generality of the discussion, initial residual stresses and strains in the liner or cladding materials have not been accounted for numerically, albeit mentioned in relation to effects of significant plastic strain.

7.4 Loading Conditions

An offshore pipeline is designed to withstand the load conditions associated with the following stages of its design life [DNV-OS-F101, 2012]:

- Transportation
- Installation
- As-laid
- Water filled
- System pressure test
- Operation
- Shut-down

For the purposes of the present study the transportation and installation phases are not relevant, since initial stresses due to these stages are disregarded. Furthermore, the as-laid and water filled conditions are similar to the shut-down condition since the weight of the pipe and its resulting curvature is not part of the discussion. The remaining conditions will be treated based on applying heat and internal pressure for relevant operational conditions.

Pipelines in operation are subjected to temperature and pressure loading. When a pipe is shut down and depressurized, however, the pressure drops fairly instantaneously, adjusting depressurization time only for the water pressure hammer effect (the water pressure hammer effect occurs in pressurized vessels with internal flow. If the vessel is closed abruptly, the inertia of the fluid content causes the flow to collide with the obstacle, causing a hammering effect) [DNV-OS-F101, 2012]. The pipeline is still fluid filled and temperature will decrease significantly more slowly than the internal pressure. Consequently, a state with operating temperature, but no internal pressure, will occur for any pipeline just after a shut-down scenario unless care is taken to depressurize sufficiently slowly for the temperature to drop at a similar rate as the pressure. In DNV-OS-F101 [2012] and API RP 1111 [2009], the shut-down condition is modeled as content filled, but with ambient temperature and shut-down pressure. Since the temperature influences the stress state in the liner, the additional consideration that the internal pressure is zero whereas the temperature is equal to the operational temperature will therefore be considered in addition to the standard approach for design of the shut-down condition.

7.5 Case Studies

Two boundary conditions will be considered. The first is an axially fixed boundary condition, which represents a buried pipe or a non-buckling pipe [DNV-RP-F110, 2007]. The second is an axially free boundary condition, which represents a pipe close to an end termination, or a pipe that is (more or less) free to expand axially due to global buckling.

Lined pipelines generally have small outer diameters due to problems with wrinkling of the liner during installation [Focke, 2007; Hilberink et al., 2011], a problem which intensifies with increasing D/t ratio. Since the liner generally has the same thickness, 2-3 mm, regardless of the dimensions of the outer steel layer, the D/t ratio for the liner increases when the diameter of the CMn cross-section increases. Consequently, the diameter of the CMn steel layer must be limited. Pipelines with cladding, however, do not have problems with wrinkling. Hence, the applicability of (more expensive) cladded pipes is not limited by their outer diameter. Therefore, when selecting relevant application examples, one fairly small and one moderately large outer diameter have been chosen in order to span a representative range of typical applications of lined and clad pipes. A more exhaustive study is recommended, but considered outside the scope of the present study. The two selected cases of representative lined or clad configurations are chosen as high temperature high pressure (HTHP) pipelines,

since these are pipeline applications for which the stress effects in the liner and backing steel due to temperature and pressure are likely to be most significant. The material properties are taken equal to those for configuration 1 in Table 1, but pipe dimensions, wall thicknesses and functional loading (temperature increase and pressures) are described in Table 3.

Table 3 – Pipe geometries and functional loading for two selected representative cases.

Application	$D_{o,b}\,[mm]$	$t_b\,[mm]$	$t\,[mm]$	$\Delta T\,[^oC]$	$p_e\,[bar]$	$p_i\,[bar]$
1	168.3	12.0	3.0	120	15	220
2	492.0	20.3	3.0	110	200	135

Application 1 represents a 6-inch (153.3-mm) internal diameter HTHP pipe with a 3-mm liner or clad layer at a water depth of approximately 150 m. Application 2 represents a 20-inch (468.7-mm) outer diameter, ultra deep water, HTHP pipe with 3-mm liner or cladding at a water depth of about 2000 m.

7.6 Application 1 – Small-Diameter Lined Pipe

The material, geometric and loading parameters are given in Table 1 and Table 3, and solutions for radial and hoop stresses are determined as a function of the radial coordinate *r* based on the analytical solutions derived and verified in this report. The results are shown in Figure 13 and Figure 14 for the two boundary conditions (axially fixed and axially free). In order to examine the individual effects of temperature and pressure, the stresses have been calculated both for pure thermal loading (i.e., no internal and external pressure) and for the combined effect of temperature and pressure.

In Figure 13 it is observed that the radial stress is fairly small, peaking at a compressive stress of only 23 MPa at the interface between the liner and the backing steel. Thus, it is likely that hoop and axial stresses will be more relevant for the capacity of the pipeline. The influence of the radial stress on a von Mises yield criterion will be investigated later in this subsection. It is also observed that there is no discernible effect of the axial boundary condition on the radial stress. This is to be expected since the stresses at the inner radius of the liner and outer radius of the backing steel are defined by the internal and external pressures acting on the inner and outer surfaces of the pipe respectively. The axial reaction therefore only influences the radial stresses via the difference in the Poisson's ratio of the two materials, and since the difference is small, the effects of the boundary conditions on the radial stress are negligible in this case.

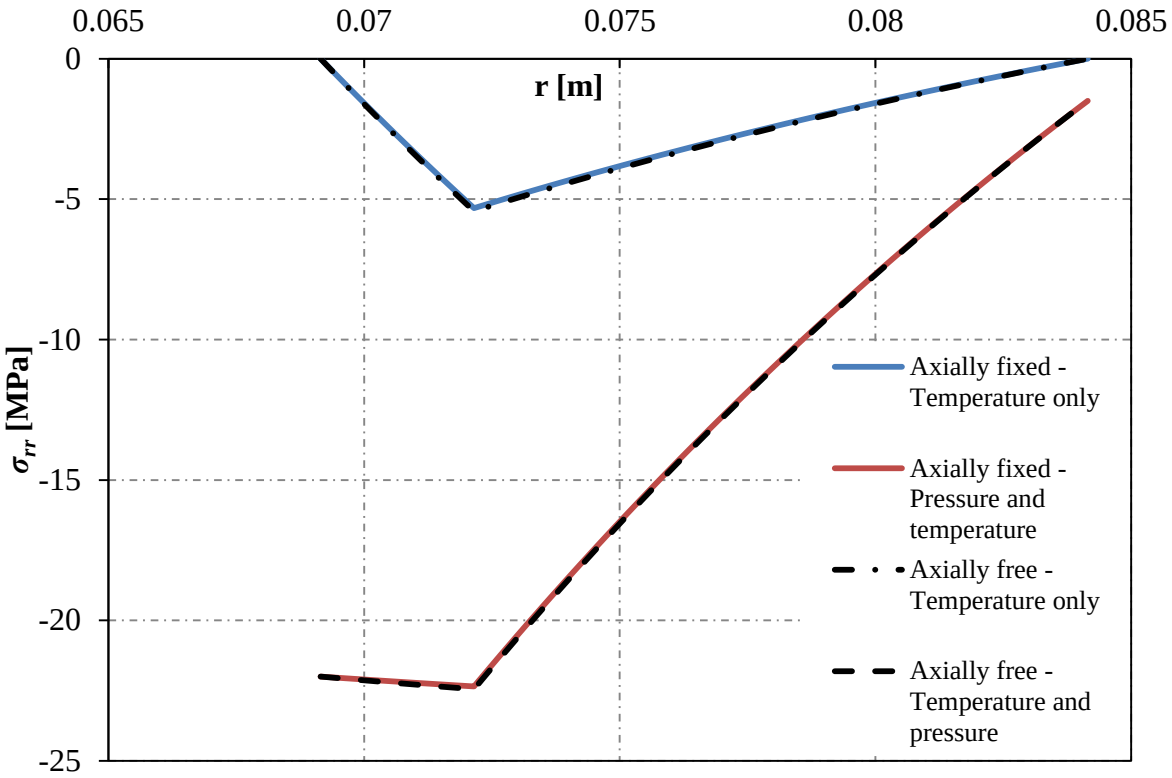

Figure 13 – Radial stresses in the CRA liner (r = 69.15 – 72.15 mm) and the CMn backing steel (r = 72.15 – 84.15 mm) for application 1, with two boundary conditions (axially fixed and axially free).

The hoop stresses are shown in Figure 14. As for the radial stresses, the hoop stresses are observed to be only negligibly dependent on the axial boundary conditions. The liner experiences slightly higher compressive hoop stresses for the axially free boundary condition, but the relative difference is only 2.0 %. Consequently, for application case 1, it can be observed that both the radial and the hoop stresses are only negligibly dependent on the axial boundary condition.

The hoop stress results presented in Figure 14 show some important features of the effect of the liner. Under pure temperature loading, the liner is in compression and the backing steel is in tension since the liner has a greater temperature expansion coefficient and is pushing on the backing steel. When the internal pressure increases, the backing steel is brought further into tension due to the combined effect of internal pressure and the temperature expansion of the liner. The case of a pipe without the liner would only include the effect of the internal pressure. The additional contact pressure resulting from thermal expansion of the liner causes the liner to act as an additional internal pressure load on the backing steel. Thus, in terms of burst failure (i.e., ultimate tensile hoop stress capacity), the liner has an adverse effect on the stress in the backing steel. However, since the typical yield

stress of offshore pipelines is around 450 MPa, it is unlikely that burst will be a governing design factor for this particular pipeline (application 1), regardless of the adverse effect from the liner.

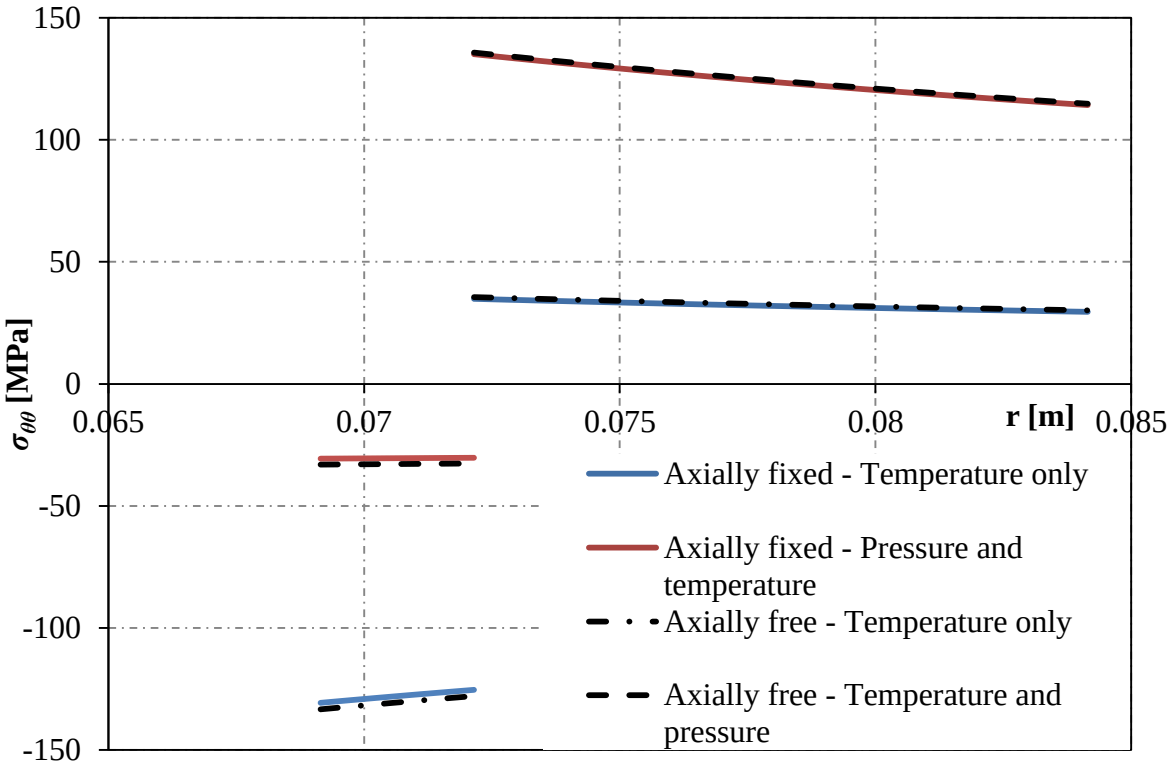

Figure 14 – Hoop stresses in the CRA liner (*r* = 69.15 – 72.15 mm) and the CMn backing steel (*r* = 72.15 – 84.15 mm) for application 1, with two boundary conditions (axially fixed and axially free).

In the solution for temperature only, it can be seen in the figure that the liner has a maximum compressive hoop stress of about 134 MPa. The liner compression will be increased further, by about 6% to a maximum of about 142 MPa, if external pressure, but no internal pressure, is added (corresponding to the loading case discussed in Section 7.4, where the pipe is depressurized but still heated). This is a very significant compressive stress, considering that the yield strength of typical liner materials is around 160-170 MPa [Marie, 2004]. When also internal pressure is applied, the compression level in the liner can be seen to be reduced. Thus, for the liner, which is in significant compression due to the temperature expansion, the high internal pressure has a positive effect on the stress levels, and depressurization of the pipe has an adverse effect on the compressive hoop stress.

It should also be noted in Figure 14 that the hoop stress in the backing steel varies little with the radial coordinate, showing for the present particular case, that the assumption in DNV-OS-F101, using the membrane hoop stress, similarly to Eq. (7), is fairly accurate. Note,

however, that the variation in backing-steel hoop stress from the peak, at the intersection between liner and backing steel, to the minimum at the outer circumference of the pipe, has 17% relative difference when both pressure and temperature are applied. Fatigue damage in offshore pipelines, according to DNV-RP-C203 [2012], shall be calculated based on stress cycles in the extreme outer fibers of the pipe. Using a standard SN-Curve approach, the fatigue damage from a stress cycle is a function of the stress to the power of either 3 or 5. With a 17% difference in stresses between the inner and outer circumference, the relative difference in fatigue damage contribution from the hoop stress is between 60% and 117%. Thus, in terms of detailed fatigue calculation from pressure or temperature cycles or both, the variation in hoop stress as a function of the radius has more significance.

Radial and hoop stresses have been presented in Figure 13 and Figure 14. In Table 4, the axial stresses in the backing steel and the liner are presented for the two boundary conditions studied, i.e., the axially fixed and the axially free boundary conditions.

Table 4 – Axial stresses in the CRA liner and the CMn backing steel, for axially fixed and axially free boundary conditions.

Load case and boundary condition	Axial stress (σ_{zz}) [MPa]	
	CRA liner	CMn backing steel
Axially fixed boundary condition		
Pressure and heat	-405	-254
Depressurized	-430	-282
Axially free boundary condition		
Pressure and heat	-134	30
Depressurized	-133	30

For the axially fixed boundary condition, typical for buried or non-buckling pipelines, it is observed that the compressive stresses in the liner are excessive, more than twice the common yield strength of such materials. Thus, for lined or clad pipes which are axially fixed, significant yield in the CRA liner or cladding can be expected. The axial compressive stresses in the backing steel are also significant, but nowhere near yield. For the axially free boundary condition, the compressive stresses in the liner arise since the backing steel is much stiffer and consequently serves as a stiff axial spring on the liner. The compressive stresses in the liner are of similar magnitude to the hoop stresses in Figure 14.

To give a better measure of the criticality of the presented application, von Mises stresses in the liner and backing steel have been calculated for each load and boundary condition combination. The von Mises stresses were calculated as a function of the radial

coordinate using Eq. (35), and for each case the peak value along the radius is presented in Table 5. For the CRA liners, a characteristic yield stress of 170 MPa has been assumed, and for the CMn backing steel, X75, a high-strength carbon steel with a yield strength of 485 MPa [DNV-OS-F101, 2012], has been assumed. It should be noted that material strength derating, which is defined in DNV-OS-F101 [2012] as a temperature-dependent reduction in the steel structural strength, has not been considered, but may be significant for a pipe with 120 degrees design temperature.

Table 5 – von Mises stress and ratio of peak von Mises stress to yield stress in liner and backing steel for axially fixed and axially free boundary conditions.

Load case and boundary condition	von Mises stress (σ_{VM}) [MPa]		Ratio to yield stress [-]	
	CRA liner	CMn backing steel	CRA liner	CMn backing steel
Axially fixed boundary condition				
Pressure and heat	536	481	3.15	0.99
Depressurized	537	386	3.16	0.80
Axially free boundary condition				
Pressure and heat	151	55	0.89	0.11
Depressurized	195	49	1.15	0.10

For each combination of load case and boundary condition, the ratio of the peak von Mises stress to the yield stress is also given in Table 5. As can be seen, the backing steel is nearly in yield in the case with the axially fixed boundary condition. This makes the current example somewhat unrealistic. The design format in an offshore standard would ensure that a realistic design is not so highly utilized. In a realistic design context, the answer to the presented utilization of the backing steel would be to add more steel in order to reduce the hoop stress from pressure, thus reducing the criticality of the design. By increasing the backing steel thickness, the criticality for the liner or cladding would likely increase since the backing steel would serve as an increasingly stiff boundary for the liner. Yielding of the liner or cladding is, however, hardly very critical, since, according to DNV-OS-F101 [2012], it is not allowed to utilize the liner or cladding as a load-carrying member in design.

The extreme conditions reflected by the high stress ratios in this case do pose some other problems. Firstly, failure of the liner itself may be characterized as a failure of the pipe, since the backing steel would not normally be designed to absorb the corrosion attack of the content fluid. Secondly, fatigue cracking in the weld between the liner and backing steel might propagate through the backing steel even if it originated from the liner. Thirdly, the liner may experience accumulated plastic strain. A pipeline will be shut down and started up

again several times during its design life, due to pigging, inspections, maintenance, etc. Thus, a number of stress cycles from start-ups and shut-downs are to be expected. The stresses in the liner are significant, indicating that large plastic strains may occur. Elasto-plastic modeling of steels is typically performed according to kinematic hardening models [Khan and Huang, 1995]. In a kinematic hardening model, a common approach is to assume that the maximum elastic stress range from tensile to compressive yield is twice the yield stress of the material, regardless of its strain history. Since the stress cycles calculated according to linear elastic theory from temperature and pressure cycles exceed twice the yield stress, as seen from Table 5, the liner is expected to yield plastically regardless of the initial stress-strain state and its strain history. As a result, the repeated start-up and shut-down cycles give rise to accumulated plastic strain. Fourthly, if a kinematic hardening model is assumed, plastic strains will occur both during loading and unloading since the full elastic stress range is exceeded in each stress cycle. Ratcheting [Jiao and Kyriakides, 2011a; 2011b], or cyclic buckling [Jiao and Kyriakides, 2009], or combinations of both may thus be potential failure modes. Finally, extreme stresses, as predicted for this particular case, will induce low cycle fatigue damage [Manson, 1966].

The study herein gives strong indications of the deformation behavior of lined and clad pipes, but (since simplifications have been made) no exact measure. Stress peaks due to thermal shocks [Marie, 2004] have not been accounted for, but could complicate the issues further. Another important effect that has been disregarded is the stiffness reduction in the liner due to plastic deformation. The tangent stiffness of the liner will decrease as the response becomes increasingly plastic, thereby reducing the impact of the liner on the stress conditions in the backing steel. Consequently, the current design practice of disregarding the liner in capacity calculations makes sense in cases where significant plastic deformation in the liner can be expected. However, the issues with low cycle fatigue may represent a direct threat to the integrity of the backing steel and should be included as a potential failure mode in offshore pipeline design contexts. As noted, there are other potential failure modes in the liner itself, which conventionally are not accounted for in pipeline design, although the present calculations clearly indicate that they may be relevant.

Other interesting observations from the results in Table 5 include the significant difference in “stress utilization" (stress ratios) in the two layers for the axially free boundary condition. It is observed that the internal pressure in the pipe is beneficial for the stress utilization in the backing steel and oppositely adverse for the stress utilization in the liner. Consequently, another indication from the study is that the current practice of not designing

for heated de-pressurized pipes may be inadequate for CRA lined or clad HTHP pipelines, particularly with respect to accumulated plastic deformation and low cycle fatigue.

The burst and collapse formulae according to DNV-OS-F101 [2012] are based on the mean hoop stress in the backing steel, disregarding the liner. The mean hoop stresses with and without the liner included are presented in Table 6 for both the pressurized and depressurized conditions in order to investigate the influence of the liner on the backing steel, and thereby the influence of the liner on the collapse and burst criteria as presently applied in DNV-OS-F101 [2012]. The mean hoop stress, when disregarding the liner or clad, has been calculated according to Eq. (7). Both the axially fixed and the axially free boundary conditions have been considered.

Table 6 – Hoop stresses in the backing steel for axially fixed and axially free boundary conditions and two loading conditions: 1) the average stress in the cylinder wall for the combined cross-section, 2) the stress in the backing steel disregarding the liner or cladding.

Load case	Mean hoop stress $\sigma_{\theta\theta}$ in the CMn backing steel [MPa]	
	Axially fixed boundary	Axially free boundary
With liner or clad		
Heated and pressurized	124	124
Heated and depressurized	24	24
Cold and depressurized	-8.4	-8.3
Disregarding liner or clad		
Pressurized	116	
Depressurized	-11	

It should be noted that Eq. (7) is independent of axial boundary conditions and temperature. As described in Section 3.1, Eq. (7) is based on static force equilibrium, and it is valid also for the combined two-layer cross-section. However, the (individual) mean hoop stress in each of the two layers may change depending on axial boundary condition and temperature. This is the reason why separate values for mean hoop stress in the backing steel are given in Table 6 for each load case and boundary condition when the liner is included. Because the Poisson's ratios of the two materials are nearly equal, the dependence of the hoop (and radial) stress on axial boundary condition is observed to be very weak, as noted also previously in Figure 13 and Figure 14. When the pipeline has a liner or cladding layer, the radial behavior is influenced by the difference in temperature expansion coefficients between the layers. When the pipe cross-section is monolithic, on the other hand, there is no influence

on the hoop stress from temperature since the pipe is free to expand radially. Thus, the results for the monolithic pipe cross-section do not vary with temperature.

From Table 6 it is observed that the hoop stress in pressurized design conditions is higher in the combined cross-section than the case where only the backing steel is considered for capacity, (i.e., when the full stress contribution is taken in the backing steel only). The reason for this behavior can be observed from Figure 14, for the load case of temperature only. The liner has a larger thermal expansion coefficient which results in a contact pressure between the layers. This contact pressure can be viewed as an added internal pressure for the backing steel causing increased tensile hoop stresses. For the combined cross-section the liner will absorb some of the stresses due to the internal pressure. For the present example, the stresses taken up by the liner from the internal pressure contribute less than the contact pressure to the backing steel from thermal expansion of the liner. Consequently, it is non-conservative, by about 6.9 % in the present case, to disregard the liner when predicting the hoop stresses in the backing steel. For the case of external overpressure in a cold pipe the opposite can be observed. When the pipe is cold, the difference in thermal expansion coefficients between the two materials has no influence and the liner has some capacity to absorb hoop stresses which reduces the hoop stresses in the backing steel.

7.7 Application 2 – Large-Diameter Clad Pipe

The material, geometric and loading parameters are given in Table 1 and Table 3, and solutions to the analytical equations for radial stress are presented in Figure 15. In this figure, the trends found from Figure 13 are observed again. The axial boundary condition has a negligible effect on the radial stresses, and the difference in thermal expansion coefficients between the steels causes a contact pressure between the layers. Since the pipeline is exposed to external overpressure, this contact pressure has an adverse effect on the clad layer, which comes further into compression, and a positive effect on the backing steel since the contact pressure acts as an additional, albeit small, internal pressure to balance the external overpressure. The magnitudes of the radial stresses are peaking at the value for the external pressure, - 20 MPa, at the position of the outer radius of the backing steel. Thus, the radial stresses are small compared to the yield stresses of the materials, and are therefore not expected to have a significant influence on the capacity of the pipeline.

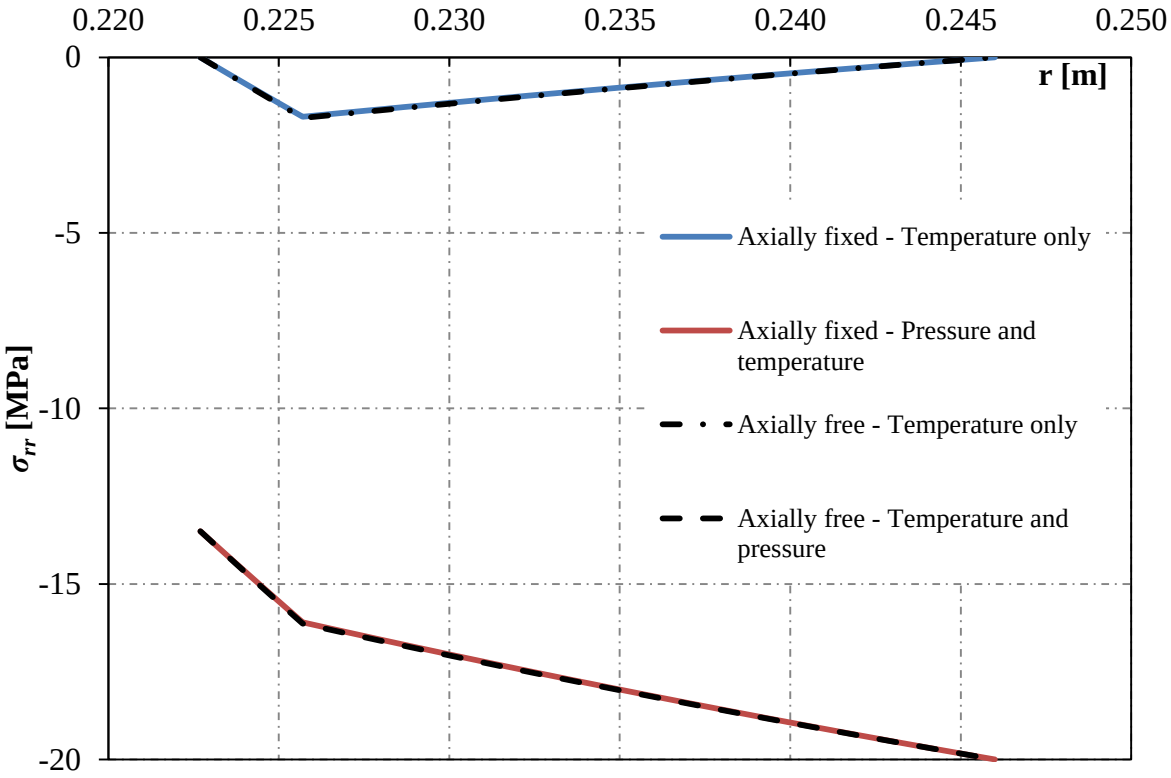

Figure 15 – Radial stresses in the CRA cladding (r = 222.7 – 225.7 mm) and the CMn backing steel (r = 225.7 – 246.0 mm) for application 2, with two boundary conditions (axially fixed and axially free).

The hoop stresses are presented in Figure 16. As observed for the radial stresses in Figure 15 and the radial and hoop stresses for application case 1 in Figure 13 and Figure 14, they are only negligibly dependent on the axial boundary conditions. The compressive hoop stresses in the cladding are higher for the axially free boundary condition, but the relative difference is only 1.3 %.

The hoop stress results presented in Figure 16 show additional important features of the effect of the clad layer. Under pure temperature loading, the cladding is in compression and the backing steel is in tension. For an external overpressure, contrary to the effects of an internal overpressure as discussed in relation to case 1, the backing steel is brought from tension to compression: This shows that in terms of collapse (i.e., ultimate external pressure capacity), the cladding has a positive, load carrying effect on the stress in the backing steel. However, since the typical yield stress of offshore pipelines is around 450 MPa, it is unlikely that collapse will be a governing design factor for this particular pipeline, regardless of the positive effect from the cladding. In terms of the temperature only solution, it is observed that the clad layer is in significant compression, peaking at 213 MPa for $r = r_i$. Already, the compressive hoop stress exceeds the yield stress for typical CRA materials. Adding only the external pressure (i.e., investigating the load case where the pipe is depressurized, but still

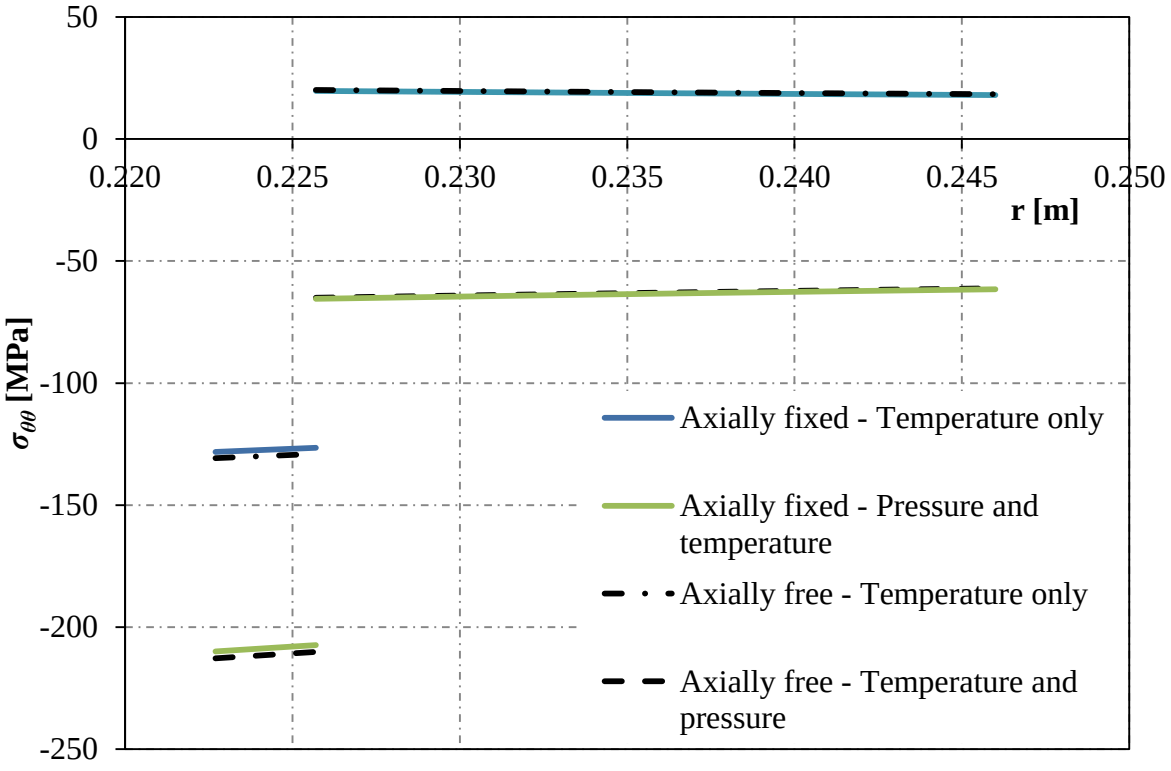

Figure 16 – Hoop stresses in the CRA cladding (*r* = 222.7 – 225.7 mm) and the CMn backing steel (*r* = 225.7 – 246.0 mm) for application 2, with two boundary conditions (axially fixed and axially free).

heated, as discussed in the introduction to Section 7.4), the maximum compressive hoop stress in the clad layer increases by a further 61 % to 343 MPa, which is about twice the typical yield strength of CRA cladding materials. Thus, for the clad layer, which is in significant compression due to temperature expansion, the high internal pressure has a positive effect on the stress levels, and depressurization of the pipe has a strong negative effect on the compressive hoop stress. It should also be noted that the observation made for application 1, that the hoop stress in the backing steel varies little with the radial coordinate, also applies for application 2. Consequently, for the present case it is fairly accurate to use the membrane hoop stress for internal and external pressure capacity assessments, as outlined in DNV-OS-F101 [2012].

In Table 7, the axial stresses in the backing steel and the cladding are presented for the two boundary conditions studied, i.e., the axially fixed and the axially free boundary conditions. For the axially fixed boundary condition, it is observed that the compressive stresses in the cladding are excessive, more than twice the common yield strength of such materials. Thus, for lined or clad pipes which are axially fixed, significant yield in the CRA liner or cladding can be expected for HTHP pipelines, as also observed for application 1. The axial compressive stresses in the backing steel are also significant, but not close to yield.

Table 7 – Axial stresses in the CRA cladding and the CMn backing steel, for axially fixed and axially free boundary conditions.

Load case and boundary condition	Axial stress (σ_{zz}) [MPa]	
	CRA cladding	CMn backing steel
Axially fixed boundary condition		
Pressure and heat	-422	-288
Depressurized	-456	-326
Axially free boundary condition		
Pressure and heat	-129	18
Depressurized	-130	18

To give a better measure of the criticality of application 2, von Mises stresses have been calculated for each load and boundary condition combination. The von Mises stresses were again calculated as a function the radial coordinate using Eq. (35), and for each case the peak value along the radius is presented in Table 8. For the CRA cladding, a characteristic yield stress of 170 MPa has been assumed, while for the CMn backing steel, X65, which is a high-strength carbon steel with a yield stress of 450 MPa [DNV-OS-F101, 2012], has been assumed. Material strength derating due to heat has been disregarded, as in Section 7.6.

Table 8 – von Mises stress and ratio of peak von Mises stress to yield stress in cladding and backing steel for axially fixed and axially free boundary conditions.

Load case and boundary condition	von Mises stress (σ_{VM}) [MPa]		Ratio to yield stress [-]	
	CRA cladding	CMn backing steel	CRA cladding	CMn backing steel
Axially fixed boundary condition				
Pressure and heat	500	355	2.94	0.79
Depressurized	581	397	3.41	0.88
Axially free boundary condition				
Pressure and heat	245	102	1.44	0.23
Depressurized	424	294	2.50	0.65

The ratio of von Mises stress to yield stress is also presented in Table 8 for each combination of load case and boundary condition. The utilization of the backing steel is high, but acceptable. Compared to application 1, application case 2 shows an even more extreme loading of the inner layer, particularly for the cases of depressurized pipe. For those cases, the von Mises stress is more than a factor two higher than the yield stress. The temperature leaves the CRA liner or cladding in compression, and so does the external pressure. Hence, the case

of external overpressure is more critical than internal overpressure for the liner or cladding material. Thus, the potential risks that were described for application 1 apply also for application 2. These risks comprise low cycle fatigue, ratcheting and cyclic buckling. Taking into account stress peaks due to thermal shocks would, as for application 1, compound the issue further. Consequently, both applications have illustrated that ratcheting, cyclic buckling and low cycle fatigue may pose risks to the integrity of buried or otherwise axially restrained HTHP pipelines with CRA liners or claddings. Application 2, where the pipe is exposed to an extremely high external overpressure, also illustrates that a utilization to yield ratio above 2 can be found in the liner or cladding even for axially unrestrained pipes.

Other interesting observations from the results in Table 8 include the significant difference in utilization between the two layers for axially free configurations, and the observation that reducing the internal pressure in the pipe is not beneficial for the utilization of the CMn backing steel, as it was for the lower water depth studied in application 1.

As mentioned previously, existing failure mode calculations in DNV-OS-F101 [2012] include burst due to internal overpressure and collapse due to external overpressure. Calculations of utilization according to DNV-OS-F101 [2012], based on the mean hoop stress in the backing steel, disregard the liner or cladding. The mean hoop stresses with and without the liner or clad layer are therefore presented in Table 9 in order to investigate the influence of the liner on the backing steel, and thereby the influence of the inner layer on the collapse and burst criteria as applied in DNV-OS-F101 [2012].

Table 9 – Hoop stresses in the backing steel for axially fixed and axially free boundary conditions and two loading conditions: 1) the average stress in the cylinder wall for the combined cross-section, 2) the stress in the backing steel disregarding the liner or cladding.

Load case	Mean hoop stress $\sigma_{\theta\theta}$ in the CMn backing steel [MPa]	
	Axially fixed boundary	Axially free boundary
With liner or clad		
Heated and pressurized	-64	-63
Heated and depressurized	-192	-192
Cold and depressurized	-211	-211
Disregarding liner or clad		
Pressurized	-94	
Depressurized	-242	

The values of mean hoop stress given in Table 9 have been calculated according to Eq. (7) for the cases where the liner or cladding has been disregarded. Both the pressurized and

depressurized load conditions have been considered. For the cases where the structural properties of the inner layer are included, both the axially fixed and the axially free boundary conditions have been examined (when the inner layer is disregarded, the mean hoop stresses are not dependent on the axial boundary condition, as seen from Eq. (7)).

From Table 9 it is observed that the hoop stress in pressurized design conditions is lower in the combined cross-section than the case where only the backing steel is considered for capacity (i.e., when the full stress contribution is taken in the backing steel only). The reason for this behavior can be observed from Figure 16, for the load case of temperature only. The liner has a larger thermal expansion coefficient which results in a contact pressure between the layers. This contact pressure can be viewed as an added internal pressure for the backing steel causing increased tensile hoop stresses. These increased tensile hoop stresses balance the high external overpressure, thereby reducing the mean hoop stress in the pipe wall. However, as was shown in Figure 16 and Table 8, the effect is opposite for the liner or cladding. This is because the thermal expansion gives compressive stresses in the liner, which are added to the effect of the external overpressure. Consequently, the depressurization has an adverse effect on the liner.

8 SUMMARY AND CONCLUSIONS

- Displacement fields of heated, pressurized two-layer cylinders have been studied in considerable detail for several boundary conditions, and corresponding analytical, exact stress solutions have been derived.
- Detailed three-dimensional FE analyses, based on an axisymmetric quarter model and a full circular model, were carried out on the two-layer cylinder for the purpose of studying potential shear interaction between the layers, and for verification purposes in general.
- The analytical stress solutions are on closed form, making them easily implementable in rules and regulations and suitable for engineering applications.
- The Lamé displacement field, deduced for cylinders subjected to internal and external pressure under plane stress and plane strain conditions, is found to be valid also for pressurized and heated layered cylinders under generalized plane strain conditions.
- Thermal expansion of corrosion-resistant alloy (CRA) liners or cladding in offshore pipelines are found to cause higher tensile hoop stresses in the pipe steel wall than presently accounted for in engineering practice.
- Start-up and shut-down cycles for CRA lined or clad pipelines cause significant stress cycles in the liners or claddings. It is argued that these may pose a risk to the integrity of such pipelines. These effects are not accounted for in current engineering practice.
- The effect of the liner on the stress situation in the backing steel is adverse for cases of internal overpressure and positive for cases with external overpressure. The behavior is opposite for the liner, i.e., external overpressure is adverse for the liner and internal overpressure is positive. The current practice of disregarding the liner when determining capacity may be non-conservative for high-temperature, high-pressure (HTHP) pipelines with internal overpressure.

ACKNOWLEDGEMENTS

The authors would like to extend their gratitude to Professor Jostein Hellesland at the University of Oslo and Dr. Olav Fyrileiv at Det Norske Veritas A/S for excellent discussions and revisions of the text.

REFERENCES

Abaqus, v. 6.12, 2012. Dassault Systèmes Simulia Corp., Providence, RI, USA.

Akcay, I.H., Kaynak, I., 2005. Analysis of multilayered composite cylinders under thermal loading. J. Reinf. Plast. Comp. 24, 1169-1179.

Ansari, R., Alisafaei, F., Ghaedi, P., 2010. Dynamic analysis of multi-layered filament-wound composite pipes subjected to cyclic internal pressure and cyclic temperature. Compos. Struct. 92, 1100-1109.

API RP 1111, 2009. Design, construction, operation and maintenance of offshore hydrocarbon pipelines (limit state design). Recommended Practice. American Petroleum Institute , API Publishing Services, Washington, DC, USA.

ASME B31.8, 2003. Gas transmission and distribution piping systems. American Society of Mechanical Engineers, New York, NY, USA.

Barbezat, G., 2005. Advanced thermal spray technology and coating for lightweight engine blocks for the automotive industry. Surf. Coat. Technol. 200 (5-6), 1990-1993.

Cook R.D., Malkus D.S, Plesha M. E., Witt R. J., 2002. Concepts and applications of finite element analysis, fourth ed. John Wiley & Sons, The University of Wisconsin, Madison, WI, USA.

Dahlquist, G., Björck, Å., 2008. Numerical methods in scientific computing, Volume I. Society for Industrial and Applied Mathematics, Philadelphia, PA, USA.

DNV-OS-F101, August 2012. Submarine Pipeline Systems. Offshore Standard. Det Norske Veritas, Høvik, Norway.

DNV-RP-F110, October 2007. Global Buckling of Submarine Pipelines. Recommended Practice. Det Norske Veritas, Høvik, Norway.

Eraslan, A.N., Akis, T., 2004. Deformation analysis of elastic-plastic two layer tubes subject to pressure: an analytical approach. Turk. J. Eng. Env. Sci. 28, 261-268.

Focke, E.S., Gresnigt, A.M., Meek, J., Nakasugi, H., 2006. The influence of heating of the liner pipe during the manufacturing process of tight fit pipe. In: Proceedings of the 16th International Offshore and Polar Engineering Conference, ISOPE 2006, San Fransisco, CA, May – June 2006, pp. 228-236.

Focke, E., 2007. Reeling of tight fit pipe, PhD thesis. Delft University of Technology, Delft, The Netherlands.

Fyrileiv, O., Collberg, L., 2005. Influence of pressure in pipeline design: Effective axial force. In: Proceedings of the 24th International Conference on Offshore Mechanics and Arctic Engineering, vol. 3, OMAE 2005-67502, Halkidiki, Greece, June 2005, pp. 629-636.

Hassan, T., Corona, E., Kyriakides, S., 1992. Ratcheting in cyclic plasticity, Part II: Multiaxial behavior. Int. J. Plast. 8 (2), 117-146.

Hilberink, A., Gresnigt A.M., Sluys, L. J., 2011. Mechanical behaviour of lined pipe during bending, numerical and experimental results compared. In: Proceedings of the 24th International Conference on Offshore Mechanics and Arctic Engineering, vol. 4, OMAE 2011-49434, Rotterdam, The Netherlands, June 2011, pp. 401-412.

Hsueh, C.H., 2002. Thermal stresses in elastic multilayer systems. Thin Solid Films 418, 182-188.

Hung, C.-I., Chen, C.K., Lee, Z.Y., 2001. Thermoelastic transient response of multilayered hollow cylinder with initial interface pressure. J. Therm. Stresses 24, 987-1006.

Jabbari, M., Sohrabpour, S., Eslami, M.R., 2002. Mechanical and thermal stresses in a functionally graded hollow cylinder due to radially symmetric loads, Int. J. Pressure Vessels Piping 79, 493-497.

Jahed, H., Farshi, B., Karimi, M., 2006. Optimum autofrettage and shrink-fit combination in multi-layer cylinders, ASME J. Pres. Ves. Technol. 128, 196-200.

Jane, K.C., Lee, Z.Y., 1999. Thermoelastic transient response of an infinitely long annular multilayered cylinder. Mech. Res. Commun. 26 (6), 709-718.

Jiao, R, Kyriakides, S., 2009. Ratcheting, wrinkling and collapse of tubes under axial cycling. Int. J. Solids Struct. 46 (14-15), 2856-2870.

Jiao, R and Kyriakides, S., 2011a. Ratcheting and wrinkling of tubes due to axial cycling under internal pressure: Part I experiments. Int. J. Solids Struct. 48 (20), 2814-2826.

Jiao, R and Kyriakides, S., 2011b. Ratcheting and wrinkling of tubes due to axial cycling under internal pressure: Part II analysis. Int. J. Solids Struct. 48 (20), 2827-2836.

Kandil, A., El-Kady, A., El-Kafrawy, A., 1995. Transient thermal stress analysis of thick-walled cylinders. Int. J. Mech. Sci., 37 (7), 721-732.

Khan, A.S., Huang, S., 1995. Continuum theory of plasticity. John Wiley & Sons, New York, Y, USA.

Kloewer, J., Behrens, R., Lettner, J., 2002. Clad Plates and Pipes in Oil and Gas Production: Applications - Fabrication – Welding. In: Proceedings of Corrosion, April 2002, Denver, CO, USA.

Lamé, G. and Clapeyron, B., 1831, Mémoire sur l'équilibre intérieur des corps solides homogènes. J. Reine Angew. Math. (Crelle's j.) 7, 145-169.

Lee, Z.Y., Chen, C.K., Hung, C.-I., 2001. Transient thermal stress analysis of multilayered hollow cylinder. Acta Mech. 151, 75-88.

Liew, K.M., Kitipornchai, S., Zhang, X.Z., Lim, C.W., 2003. Analysis of the thermal stress behaviour of functionally graded hollow circular cylinders. Int. J. Solids Struct. 40, 2355-2380.

Manson, S.S., 1966. Thermal stress and low cycle fatigue. McGraw-Hill, The University of Michigan, MI, USA.

Marie, S., 2004. Analytical expression of the thermal stresses in a vessel or pipe with cladding submitted to any thermal restraint. Int. J. Pressure Vessels Piping 81, 303-312.

NORSOK standard M-001, 2004. Materials selection, rev. 4. Standards Norway, Lysaker, Norway.

Olsson, J., Grützner, H., 1989. Experiences with a high-alloyed stainless steel under highly corrosive conditions. Mater. Corros. 40 (5), 279-284.

Ootao, Y., Tanigawa, Y., 2006. Transient thermoelastic analysis for a functionally graded hollow cylinder. J. Therm. Stresses 29, 1031-1046.

Parker, A.P., 2001. Autofrettage of open-end tubes – pressures, stresses, strains and code comparisons. ASME J. Pres. Ves. Technol. 123, 271-281.

Perry, J., Aboudi, J., 2003. Elasto-plastic stresses in thick walled cylinders ASME J. Pres. Ves. Technol. 125, 248-252.

Radu, V., Taylor, N., Paffumi, E., 2008. Development of new analytical solutions for elastic thermal stress components in a hollow cylinder under sinusoidal transient thermal loading. Int. J. Pressure Vessels Piping 85, 885-893.

Shao, Z.S., 2005. Mechanical and thermal stresses of a functionally graded circular hollow cylinder with finite length. Int. J. Pressure Vessels Piping 82, 155-163.

Shi, Z., Zhang, T., Xiang, H., 2006. Exact solutions of heterogeneous elastic hollow cylinders. Compos. Struct. 79, 140-147.

Smith, L.M., 2012. Engineering with clad steel, second ed. Technical Series No. 10064, The Nickel Institute, Brussels, Belgium.

Sparks, C.P., 1984. The influence of tension, pressure and weight on pipe and riser deformations and stresses. ASME J. Energy Resour. Technol. 106, 46-54.

Timoshenko, S.P., 1958. Strength of materials, part II, third ed. D. Van Nostrand Company, Princeton, NJ, USA.

Vedeld, K., Osnes, H., Fyrileiv, O., 2012a. Analytical expressions for stress distributions in lined pipes: Axial stress and contact pressure interaction. Marine Struct. 26 (1), 1-26.

Vedeld, K., Osnes, H., Fyrileiv, O., 2012b. New interpretations of gripping force tests for lined pipes. Marine Struct. 29 (1), 152-168.

Weierstrass, K., 1903. Über die analytische Darstellbarkeit sogenannter willkürlicher Funktionen einer reeller Veränderlichen. In: Weierstrass, K., Mathematische Werke, vol. 3. Mayer and Müller, Berlin, pp. 1-37.

Wilson, W.R.D., Skelton, W.J., 1967. Design of bi-metallic high pressure cylinders. In: Proceedings of the Institution of Mechanical Engineers, vol. 182 (3), Conference Proceedings, September 1967, pp. 1-10.

Xiang, H., Shi, Z., Zhang, T., 2006. Elastic analyses of heterogeneous hollow cylinders. Mech. Res. Commun. 33, 681-691.

Zhang, Q. Wang, Z.W., Tang, C.Y, Hu, D.P, Xia, L.Z., 2012. Analytical solution of the thermo-mechanical stresses in a multilayered composite pressure vessel considering the influence of closed ends. Int. J. Pressure Vessels Piping 98, 102-110.

APPENDIX A – Applicability of the Lamé Displacement Field

A.1 Investigation of the Displacement Field for Layered Cylinders under Generalized Plane Strain Conditions

The Lamé displacement field given by Eq. (14) for a cylinder subjected to radial pressure is, as seen in Section 3.1, based on an assumption of plane stress or plane strain. For the case of generalized plane strain and direct axial loading, illustrated by Figure 2 b), the stress and strain states are three-dimensional, and the assumptions of plane stress or plane strain are no longer valid. It was argued in Section 3.2 that the radial displacement field given by Eq. (14) would still be valid and exact. A thorough investigation of this matter, i.e., the applicability of the Lamé displacement field for cylinders subjected to both direct axial loading and temperature in addition to uniform radial pressure, is presented in the current Appendix A.

To investigate whether the Lamé displacement field, Eq. (14), is accurate or not for all load and boundary conditions to be considered, a more general displacement field assumption given by

$$\begin{aligned} u_{r,\exp} &= \sum_{i=-n}^{n} C_{ri} r^i \\ u_\theta &= 0 \end{aligned} \qquad \textbf{(57)}$$

is applied first. Here, $u_{r,exp}$ is the general (expanded) displacement field in the radial direction. Due to the axial symmetry of the system and loading conditions, the displacement u_θ in the hoop direction is identically zero over the whole solution domain. Note that if n = 1, we obtain the Lamé displacement field with the addition of a constant term. The axial displacement component is, as shown in Section 3.2, given by

$$u_z = C_z \frac{z}{L} \qquad \textbf{(58)}$$

If we assume that the exact solution is continuous, the displacement assumption in Eq. (57), will converge towards the exact solution according to Weierstrass' approximation theorem since the cylinder layers are of finite radii, and consequently, defined on a compact subspace of **R**, where **R** denotes the space of real numbers [Weierstrass, 1903]. Note, however, that the fraction terms, i.e., the terms $C_{ri} \cdot r^i$ where $i < 0$, are linearly dependent in the subspace spanned by the monomial basis, where the monomial basis is $\{r^i\}_{i=0}^{\infty}$. Therefore, it is expected that the stiffness matrix at some point will become singular for some large value of

n, since the fraction terms will result in a near over-determined set of equations. In other words, the displacement assumption spans the solution space if we allow *n* to go to infinity, but we have too many equations, and hence we expect singularity, i.e., condition number problems for large *n*. It is to be expected, however, that a large *n* value will not be necessary for achieving convergence, since the solution for cylinders without axial loading requires only $n = 1$.

Since heat and direct axial loading are applied uniformly, and the axial strains, according to Eq. (4), per definition are uniform over the cross-section, the load conditions from cases a) and b) in Figure 2 yield uniform axial stress along the length of the cylinders. Furthermore, it makes no difference to the solution whether a pressure is a contact pressure from an adjacent layer or an applied pressure at a free boundary. Thus, a displacement field providing an exact solution for a one-layer cylinder under axial load and internal and external pressure will be applicable for each individual layer in a multi-layer cylinder. Therefore it is sufficient to demonstrate the validity of the Lamé displacement field, Eq. (14), for a single layer exposed to axial loading and internal and external pressure. This is achieved by assuming the general displacement field in Eq. (57), and showing that the only non-zero coefficients in the result are exactly those included in the Lamé displacement field, Eq. (14), for a one-layer cylinder. The theory used for computing numerical results is reviewed below.

The general displacement assumption in Eq. (57) written on matrix form becomes

$$\begin{aligned} \mathbf{u} &= \begin{bmatrix} u_{r,\exp} \\ u_z \end{bmatrix} = \mathbf{N}\mathbf{D}, \\ \mathbf{N} &= \begin{bmatrix} \mathbf{N}_r & 0 \\ \mathbf{0} & N_z \end{bmatrix} \end{aligned} \tag{59}$$

where **u** is the displacement field vector. **D** is the generalized displacement vector and **N** is the shape function matrix defined by

$$\begin{aligned} \mathbf{N}_r &= \begin{bmatrix} r^{-n} & \dots & r^{-1} & 1 & r & \dots & r^n \end{bmatrix} \\ N_z &= \begin{bmatrix} \dfrac{z}{L} \end{bmatrix} \\ \mathbf{D}^T &= \begin{bmatrix} C_{r(-n)} & \dots & C_{r(-1)} & C_{r0} & C_{r1} & \dots & C_{rn} & C_z \end{bmatrix} \end{aligned} \tag{60}$$

The strain field in cylindrical coordinates [Cook et al. 2002] is given by

$$
\begin{aligned}
\varepsilon_{rr} &= \frac{\partial u_{r,\exp}}{\partial r} = \sum_{i=-n}^{n} C_{ri} i r^{i-1} \\
\varepsilon_{\theta\theta} &= \frac{1}{r}\frac{\partial u_\theta}{\partial \theta} + \frac{1}{r} u_r = \sum_{i=-n}^{n} C_{ri} r^{i-1} \\
\varepsilon_{zz} &= \frac{\partial u_z}{\partial z} = \frac{C_z}{L} \\
\gamma_{r\theta} &= \frac{1}{r}\frac{\partial u_{r,\exp}}{\partial \theta} + \frac{\partial u_\theta}{\partial r} - \frac{u_\theta}{r} = 0 \\
\gamma_{\theta z} &= \frac{\partial u_\theta}{\partial z} + \frac{1}{r}\frac{\partial u_z}{\partial \theta} = 0 \\
\gamma_{rz} &= \frac{\partial u_{r,\exp}}{\partial z} + \frac{\partial u_z}{\partial r} = 0
\end{aligned}
\tag{61}
$$

where ε_{ij} are normal strains and γ_{ij} are shear strains. Since the shear strains are all zero, the strain field simplifies to

$$
\boldsymbol{\varepsilon} = \begin{bmatrix} \varepsilon_{rr} \\ \varepsilon_{\theta\theta} \\ \varepsilon_{zz} \end{bmatrix} \tag{62}
$$

Based on the strain field in Eq. (61), the following differential operator is established:

$$
\mathbf{d} = \begin{bmatrix} \dfrac{\partial}{\partial r} & 0 \\ \dfrac{1}{r} & 0 \\ 0 & \dfrac{\partial}{\partial z} \end{bmatrix} \tag{63}
$$

Based on the nomenclature introduced by Eqs. (59), (61) and (63), the strain field can then be expressed in matrix notation as

$$
\boldsymbol{\varepsilon} = \mathbf{BD} = \mathbf{dND} \tag{64}
$$

An expression for **B** can be found by applying the operator **d** to **N**:

$$
\mathbf{B} = \mathbf{dN} = \begin{bmatrix} \mathbf{N}_{r,r} & 0 \\ \dfrac{\mathbf{N}_r}{r} & 0 \\ \mathbf{0} & N_{z,z} \end{bmatrix} \tag{65}
$$

Here, the standard comma-notation is used for partial differentiation. Thus, the subscripts "$,r$" and "$,z$" means differentiation with respect to the variables r or z, respectively.

By use of the principle of minimum potential energy, the system stiffness relationship, given by **KD** = **R,** can be derived in standard fashion [Cook et al., 2002]. Here, **R** is the load

vector and **K** is the system (global) stiffness matrix that can be given in the following well known form [Cook et al., 2002]:

$$\mathbf{K} = \int_V \mathbf{B}^T \mathbf{E} \mathbf{B} \, dV \tag{66}$$

Here, V is the volume of the body and **E** is the three-dimensional material stiffness matrix (generalized Young's modulus) as defined, in the case with principal stresses, by

$$\mathbf{E} = \hat{E} \begin{bmatrix} 1-\nu & \nu & \nu \\ \nu & 1-\nu & \nu \\ \nu & \nu & 1-\nu \end{bmatrix}, \quad \hat{E} = \frac{E}{(1-2\nu)(1+\nu)} \tag{67}$$

where E is the Young's modulus and ν is the Poisson's ratio. By inserting for **B** and **E** from Eqs. (65) and (67), Eq. (66) the following expression is obtained for the stiffness matrix:

$$\mathbf{K} = \int_V \begin{bmatrix} (1-\nu)\mathbf{N}_{r,r}^T \mathbf{N}_{r,r} + \frac{\nu}{r}\left(\mathbf{N}_{r,r}^T \mathbf{N}_r + \mathbf{N}_r^T \mathbf{N}_{r,r}\right) + \frac{(1-\nu)}{r^2}\mathbf{N}_r^T \mathbf{N}_r & \nu N_{z,z}\left(\mathbf{N}_{r,r}^T + \frac{\mathbf{N}_r^T}{r}\right) \\ \nu N_{z,z}\left(\mathbf{N}_{r,r} + \frac{\mathbf{N}_r}{r}\right) & (1-\nu) N_{z,z}^2 \end{bmatrix} dV \tag{68}$$

The load vector **R**, which in the principle of minimum potential energy follows from the work done by the internal and external pressures over the internal and external surfaces of the pipe, respectively, and the work of the distributed axial load at the end of the cross-section, can be written as follows:

$$\begin{aligned} \mathbf{R} = \int_S \mathbf{N}^T \Phi \, dS &= \int_{S_i} \begin{bmatrix} \mathbf{N}_r^T & \mathbf{0} \\ 0 & N_z \end{bmatrix} \begin{bmatrix} p_i \\ 0 \end{bmatrix} dS_i + \int_{S_o} \begin{bmatrix} \mathbf{N}_r^T & \mathbf{0} \\ 0 & N_z \end{bmatrix} \begin{bmatrix} -p_e \\ 0 \end{bmatrix} dS_o \\ + \int_{A_s} \begin{bmatrix} \mathbf{N}_r^T & \mathbf{0} \\ 0 & N_z \end{bmatrix} \begin{bmatrix} 0 \\ N / A_s \end{bmatrix} dA_s &= 2\pi L \begin{bmatrix} \left(p_i r_i^{-n+1} - p_e r_o^{-n+1}\right) \\ \vdots \\ \left(p_i - p_e\right) \\ \left(p_i r_i - p_e r_o\right) \\ \left(p_i r_i^2 - p_e r_o^2\right) \\ \vdots \\ \left(p_i r_i^{n+1} - p_e r_o^{n+1}\right) \\ \frac{N}{2\pi L} \end{bmatrix} \end{aligned} \tag{69}$$

where Φ is a vector of surface pressures (tractions), p_i and p_e are defined in Figure 2 and the surfaces S_i, S_o and A_s are defined in Figure A.1.

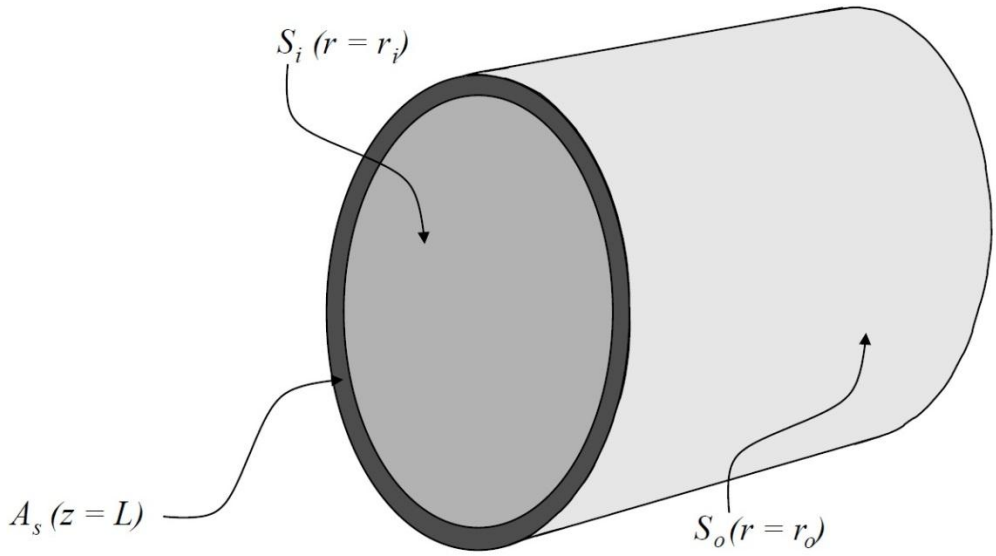

Figure A.1 – Definition of cylinder surfaces.

The theory presented above will now be used to compute numerical results for the purpose of determining the effect of including more than the two Lamé terms in the displacement field. The displacement field coefficients (constants) are calculated for increasing n values (where n is the index defined in Eq. (57)) for one specific single-layer case example. This example is taken equal to the cylinder defined by the outer layer of the case labeled "configuration 1" in Table 1 of Section 6.1. In addition to the loads defined in Table 1, an axial force of N = 1 MN is applied.

The displacement fields for n = 1, 2 and 3 become

$$\begin{aligned} n=1:&\quad u_{r,\exp} = C_{r(-1)}\frac{1}{r} + C_{r0} + C_{r1}r \\ n=2:&\quad u_{r,\exp} = C_{r(-2)}\frac{1}{r^2} + C_{r(-1)}\frac{1}{r} + C_{r0} + C_{r1}r + C_{r2}r^2 \\ n=3:&\quad u_{r,\exp} = C_{r(-3)}\frac{1}{r^3} + C_{r(-2)}\frac{1}{r^2} + C_{r(-1)}\frac{1}{r} + C_{r0} + C_{r1}r + C_{r2}r^2 + C_{r3}r^3 \end{aligned} \tag{70}$$

where the displacement field coefficients, resulting from the computations, are presented in Table A.1.

For n = 1, it is observed that the Lamé field results, since the constant term C_{r0} becomes zero and only the two coefficients remain. The same trend can be observed for n = 2. The constant, the quadratic and the inverse quadratic terms vanish and only the two Lamé coefficients remain. For n = 3, however, it is observed that the quadratic term coefficient C_{r2} is non-zero, albeit very small. In this case, the condition number for the stiffness matrix was in the order of magnitude $5 \cdot 10^{-18}$ and the accuracy of the solution therefore becomes poor. For

higher *n*, the numerical solution breaks down due to poor conditioning of the stiffness matrix, and the solution diverges from the exact solution. It is highly likely that the poor conditioning of the stiffness matrix is a result of non-contributing displacement coefficients. It was expected that conditioning would become an issue for large *n* values since the fraction terms are linearly dependent on the monomial basis if *n* goes to infinity. The singularity issues experienced in this case are, however, entirely unrelated to this problem since the solution breaks down even for small *n* values. Consequently, the fact that the coefficients are calculated to zero, or very near zero, seems to be the issue, and not that the fraction terms are linearly dependent on the much larger solution space spanned by the monomial basis.

Table A.1 – Coefficients for the displacement field

$10^4 \cdot$ coefficient	$n = 1$	$n = 2$	$n = 3$
$C_{r(-3)}$	-	-	0.0000
$C_{r(-2)}$	-	-0.0000	0.0000
$C_{r(-1)}$	0.1244	0.1244	0.1244
C_{r0}	-0.0000	-0.0000	-0.0000
C_{r1}	0.2923	0.2923	0.2923
C_{r2}	-	0.0000	0.0001
C_{r3}	-	-	-0.0000
C_z	-0.0535	-0.0535	-0.0535

The results presented and discussed above strongly indicate that the Lamé displacement field (with two constants) in the radial direction is exact also for axially loaded cylinders. Even so, a formal proof is given below that confirms that the result holds generally.

A.2 Formal Proof for the Validity of the Lamé Displacement Field for Layered Cylinders under Generalized Plane Strain Conditions

We assume that the axially loaded cylinder is hollow, and consequently that $r_i > 0$. The domain of our solution is then the compact subspace of $\mathbf{R}$ $[r_i, r_o]$. Note that the Lamé displacement field is not defined for $r_i = 0$, and that the proof therefore requires $r_i > 0$. Before the proof can be completed, some partial results are necessary. First, we determine the displacement field coefficients for an axially loaded and pressurized cylinder when the Lamé displacement field is applied. This is easily accomplished by setting $n = 1$ in Eq. (60) and setting the constant term $C_{r0} = 0$. By inserting these into Eqs. (68) and (69), the following expressions for the stiffness matrix and load vector are obtained:

$$\mathbf{K} = \hat{E}\begin{bmatrix} 2\pi L(1-2\nu)\left(\dfrac{1}{r_i^2}-\dfrac{1}{r_o^2}\right) & 0 & 0 \\ 0 & 2LA_s & 2\nu A_s \\ 0 & 2\nu A_s & \dfrac{A_s(1-\nu)}{L} \end{bmatrix}$$
$$\mathbf{R}^T = \begin{bmatrix} 2\pi L(p_i - p_e) & 2\pi L(p_i r_i^2 - p_e r_o^2) & N \end{bmatrix} \quad \textbf{(71)}$$

The displacement field coefficients can now be solved for from the stiffness relationship (**KD = R**) and written as follows:

$$\mathbf{D} = \begin{bmatrix} C_{r(-1)} \\ C_{r1} \\ C_z \end{bmatrix} = \mathbf{K}^{-1}\mathbf{R} = \begin{bmatrix} \dfrac{r_i^2 r_o^2 (p_i - p_e)(1+\nu)}{E(r_o^2 - r_i^2)} \\ \dfrac{(p_i A_i - p_e A_e)(1-\nu) - \nu N}{EA_s} \\ \dfrac{N - 2\nu(p_i A_i - p_e A_e)}{EA_s} L \end{bmatrix} \quad \textbf{(72)}$$

By setting the axial load $N = 0$, it is observed that the expressions for $C_{r(-1)}$ and C_{r1} are identical to the corresponding expressions in Eq. (17).

For the purpose of the proof of the adequacy of the Lamé displacement field, the exact displacement field solution will be termed $u_{r,exact}$. The proof will be conducted by falsification, i.e., we will assume that the Lamé displacement field is not equal to $u_{r,exact}$ and show that this leads to a contradiction. If $u_r \neq u_{r,exact}$, then:

$$u_{r,exact} - u_r = \rho(r) \quad \textbf{(73)}$$

where $\rho(r)$ is the the error in the Lamé approximation which is non-zero for some subset of the domain $[r_i, r_o]$. We know that the monomial basis $\{1, r, r^2, \ldots\}$ is a basis for the space **C** of all continuous functions, on any compact subspace of **R.** The error function $\rho(r)$ is continuous since $u_{r,exact}$ and u_r are obviously continuous. Thus, $\rho(r)$ can be expressed by a linear combination of basis vectors from the monomial basis $\{1, r, r^2, \ldots\}$, i.e., $\rho(r)$ can be expressed as a polynomial since it is continuous and its domain is compact on **R**. In the following, we will denote the scalar coefficient of the error function from the arbitrary basis vector r^k as C_{rk}, where

$$k \in \{0,2,3,4,...\}, \quad \textbf{(74)}$$

i.e., the subset of all non-negative integers, with the exception of $\{1\}$ since C_{r1} is already contained in u_r. Since we have assumed that u_r is different from $u_{r,exact}$ for some k, C_{rk} must be the first non-zero component. Then we expand the Lamé displacement field u_r by an

additional term $C_{rk}\cdot r^k$. The expanded displacement field will be inserted into Eqs. (68) and (69) for assessment of the contribution from the term $C_{rk}\cdot r^k$ to the error function $\rho(r)$.

We define the shape function matrix $\mathbf{N}_r$ and displacement vector $\mathbf{D}$ by

$$\begin{aligned}\mathbf{N}_r &= \begin{bmatrix} r^{-1} & r & r^k \end{bmatrix} \\ N_z &= \begin{bmatrix} \frac{z}{L} \end{bmatrix} \\ \mathbf{D}^T &= \begin{bmatrix} C_{r(-1)} & C_{r1} & C_{rk} & C_z \end{bmatrix}\end{aligned} \tag{75}$$

Inserting these into Eqs. (68) and (69), and performing the integrations over the volume and boundary surfaces, the following expressions are obtained for the stiffness matrix $\mathbf{K}$ and load vector $\mathbf{R}$:

$$\begin{aligned}\mathbf{K} &= 2\pi\hat{E}\begin{bmatrix} L(1-2\nu)\left(\frac{1}{r_i^2}-\frac{1}{r_o^2}\right) & 0 & L(1-2\nu)\left(r_i^{k-1}-r_o^{k-1}\right) & 0 \\ 0 & L\left(r_o^2-r_i^2\right) & L\left(r_o^{k-1}-r_i^{k-1}\right) & \nu\left(r_o^2-r_i^2\right) \\ L(1-2\nu)\left(r_i^{k-1}-r_o^{k-1}\right) & L\left(r_o^{k+1}-r_i^{k+1}\right) & \frac{EL\left(r_o^{2k}-r_i^{2k}\right)\left(1+k^2+k^2\nu+2k\nu-\nu\right)}{k} & \nu\left(r_o^{k+1}-r_i^{k+1}\right) \\ 0 & \nu\left(r_o^2-r_i^2\right) & \nu\left(r_o^{k+1}-r_i^{k+1}\right) & \frac{A_s(1-\nu)}{2\pi L} \end{bmatrix} \\ \mathbf{R}^T &= \begin{bmatrix} 2\pi L(p_i-p_e) & 2\pi L\left(p_i r_i^2-p_e r_o^2\right) & 2\pi L\left(p_i r_i^{k+1}-p_e r_o^{k+1}\right) & N \end{bmatrix}\end{aligned} \tag{76}$$

Note that k in Eq. (76) is greater than zero. For the case of $k = 0$, the integrations require special attention, and is considered below in Eq. (79). Since the displacement functions defined in Eq. (75) are linearly independent, the stiffness matrix $\mathbf{K}$ is non-singular. Consequently, only one solution of the stiffness equation $\mathbf{KD} = \mathbf{R}$ is possible. We try the solution determined for the Lamé field in Eq. (72), i.e.

$$\mathbf{D} = \begin{bmatrix} \frac{r_i^2 r_o^2 (p_i-p_e)(1+\nu)}{E\left(r_o^2-r_i^2\right)} \\ \frac{(p_i A_i - p_e A_e)(1-\nu)-\nu N}{EA_s} \\ 0 \\ \frac{N-2\nu(p_i A_i - p_e A_e)}{EA_s} L \end{bmatrix} \tag{77}$$

By multiplying the assumed value of $\mathbf{D}$ with the stiffness matrix $\mathbf{K}$, we arrive at the following load vector $\mathbf{R}$:

$$\mathbf{R}^T = \begin{bmatrix} 2\pi L(p_i-p_e) & 2\pi L\left(p_i r_i^2-p_e r_o^2\right) & 2\pi L\left(p_i r_i^{k+1}-p_e r_o^{k+1}\right) & N \end{bmatrix} \tag{78}$$

Since $\mathbf{R}$ in Eq. (78) is exactly equal to the load vector determined above and given in Eq. (76), the displacement vector proposed in Eq. (77) represents an exact solution of the system of

equations **KD** = **R**. Consequently, the factor C_{rk} must be zero, and therefore the assumption that $\rho(r)$ is non-zero must be false.

Now it remains to show that this conclusion holds also for $k = 0$. Repetition of the exercise for $k = 0$ yields the following expressions for the stiffness matrix and load vector:

$$\mathbf{K} = 2\pi\hat{E}\begin{bmatrix} L(1-2\nu)\left(\frac{1}{r_i^2}-\frac{1}{r_o^2}\right) & 0 & L\frac{(1-2\nu)(r_o-r_i)}{r_i r_o} & 0 \\ 0 & L(r_o^2-r_i^2) & L(r_i-r_o) & \nu(r_o^2-r_i^2) \\ L\frac{(1-2\nu)(r_o-r_i)}{r_i r_o} & L(r_i-r_o) & L(1-\nu)(\ln r_o-\ln r_i) & \nu(\acute{}r_o-r_i) \\ 0 & \nu(r_o^2-r_i^2) & \nu(\acute{}r_o-r_i) & \frac{A_s(1-\nu)}{2\pi L} \end{bmatrix} \qquad \textbf{(79)}$$

$$\mathbf{R}^T = \begin{bmatrix} 2\pi L(p_i-p_e) & 2\pi L(p_i r_i^2 - p_e r_o^2) & 2\pi L(p_i r_i - p_e r_o) & N \end{bmatrix}$$

Again, by multiplying this **K** matrix with the proposed solution in Eq. (77), the load vector **R** in Eq. (79) is obtained. The contribution to the error function from the term corresponding to $k = 0$ must therefore be zero, in contradiction to the assumption that $\rho(r)$ is non-zero. From the arguments above, the error function has no contributions from polynomial terms of order {0, 2, 3, 4, …}, and hence the error function $\rho(r)$ is identically zero. Thereby it has been shown that the Lamé field is exact for each individual layer in an axially loaded, multi-layer cylinder.

APPENDIX B – Comparison with FE Results for Radial and Hoop Stresses

The analytical formulae for stress distributions in two-layer cylinders derived in the present study were verified by comparison to results of detailed FE analyses, as described in Section 6. Two configurations with properties as shown in Table 1 were applied for the validation study. The following five analyses were performed:

1. Configuration 1 – fully restrained axially (plane strain)
2. Configuration 1 – axially free (generalized plane strain), i.e. $K = 0$ and $N = 0$
3. Configuration 2 – fully restrained axially (plane strain)
4. Configuration 2 – axially free (generalized plane strain), i.e. $K = 0$ and $N = 0$
5. Configuration 2 – spring-mounted (generalized plane strain) with $K = 10^{10}$ N/m and $N = -4.505 \cdot 10^{5}$ N

Only selected results were shown in Section 6.3. For completeness, all the resulting radial and hoop stress comparisons are presented in this appendix. The axial stresses are not shown, since these were presented in Section 6.3.

B.1 Configuration 1 - Axially Restrained

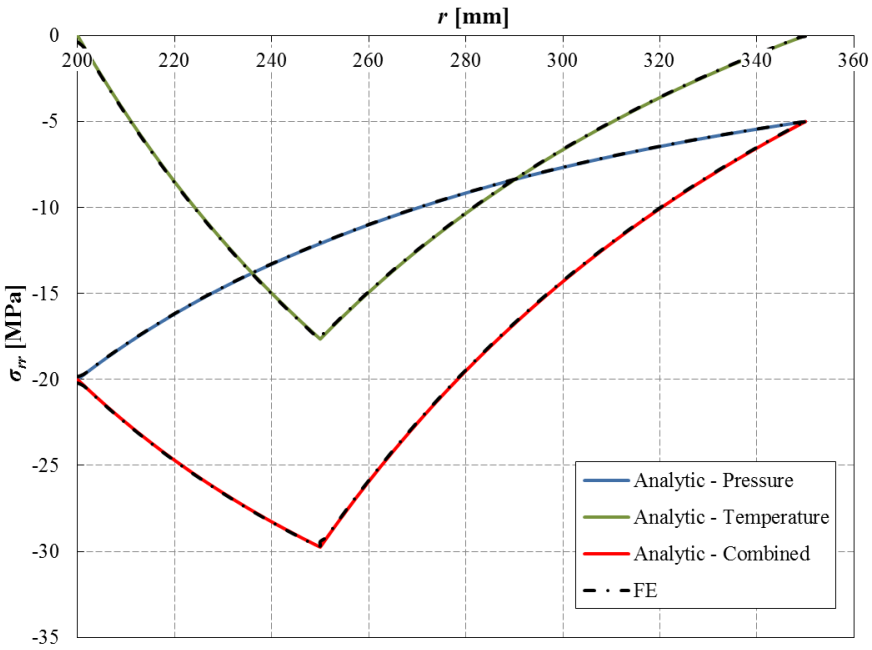

Figure B.1 – Analytically derived radial stresses as a function of the radial coordinate *r* for configuration 1 (Table 1) in axially restrained condition with pressure loading (blue line), temperature loading (green line) and combined pressure and temperature loading (red line). FE results are shown as black dash-dot lines.

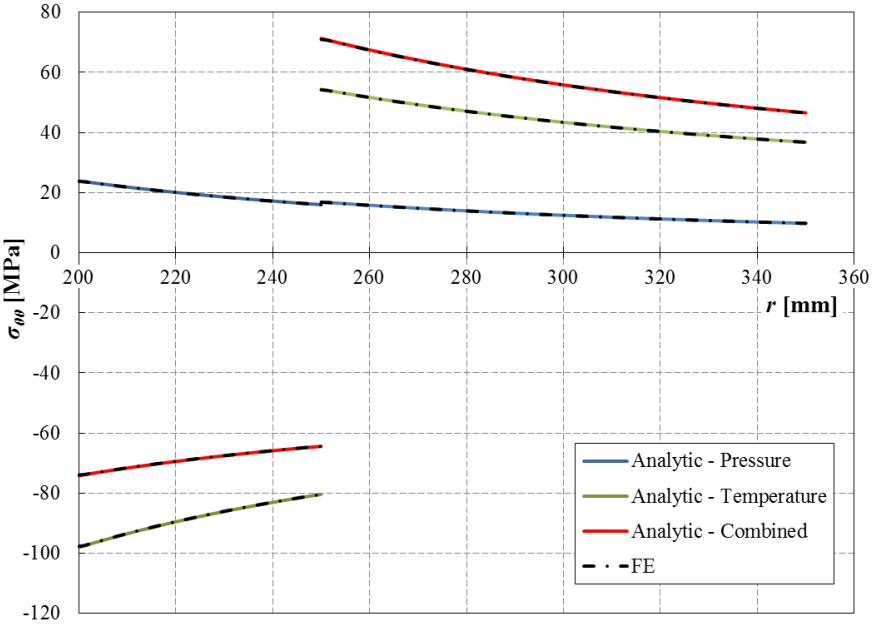

Figure B.2 – Analytically derived hoop stresses as a function of the radial coordinate *r* for configuration 1 (Table 1) in axially restrained condition with pressure loading (blue line), temperature loading (green line) and combined pressure and temperature loading (red line). FE results are shown as black dash-dot lines.

B.2 Configuration 1 - Axially Free

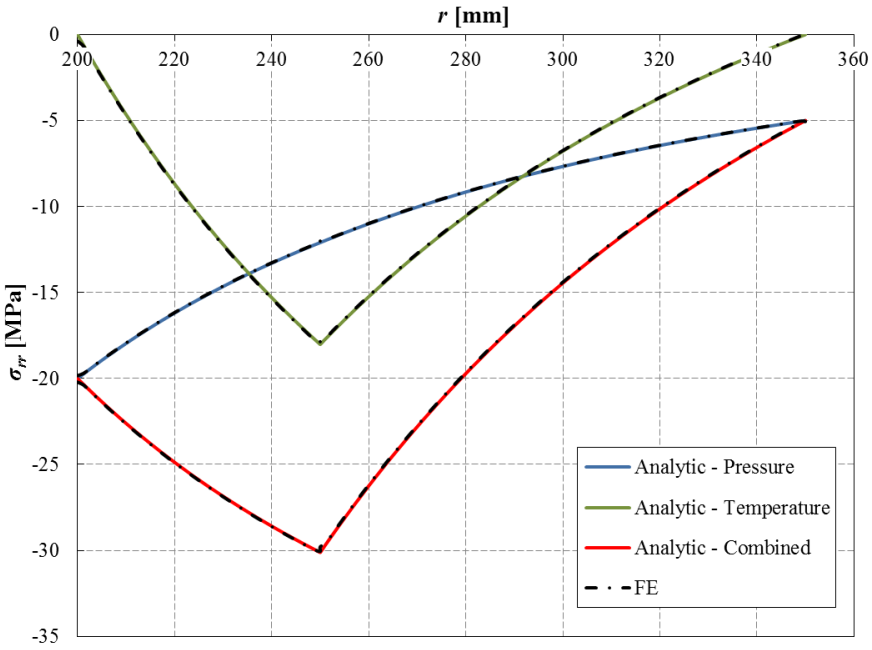

Figure B.3 – Analytically derived radial stresses as a function of the radial coordinate *r* for configuration 1 (Table 1) in axially free condition with pressure loading (blue line), temperature loading (green line) and combined pressure and temperature loading (red line). FE results are shown as black dash-dot lines.

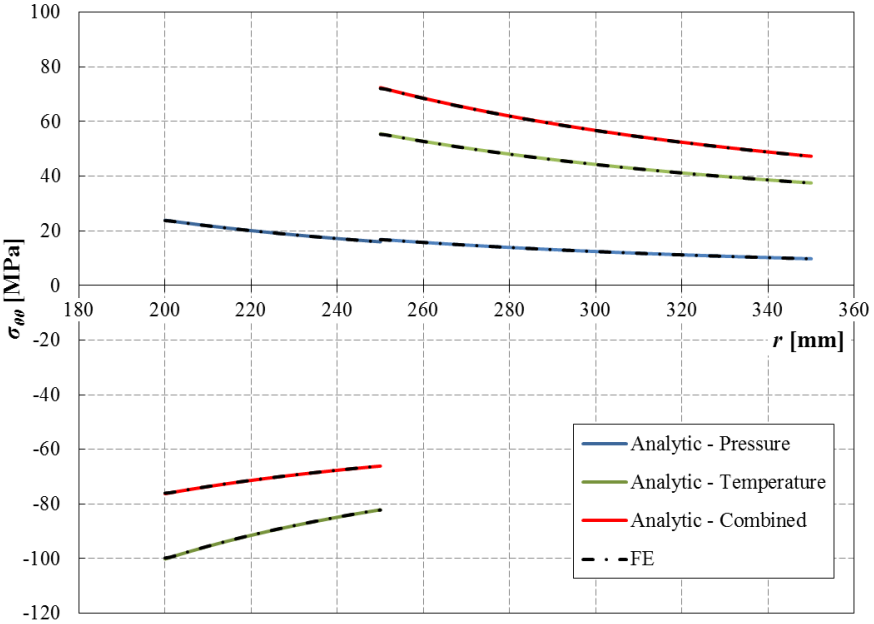

Figure B.4 – Analytically derived hoop stresses as a function of the radial coordinate *r* for configuration 1 (Table 1) in axially free condition with pressure loading (blue line), temperature loading (green line) and combined pressure and temperature loading (red line). FE results are shown as black dash-dot lines.

B.3 Configuration 2 - Axially Restrained

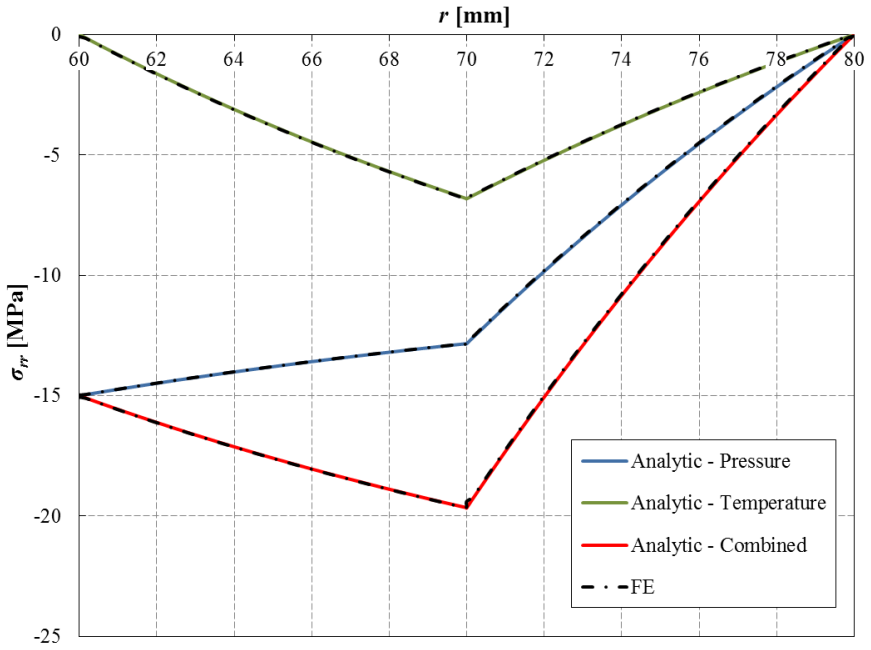

Figure B.5 – Analytically derived radial stresses as a function of the radial coordinate *r* for configuration 2 (Table 1) in axially restrained condition with pressure loading (blue line), temperature loading (green line) and combined pressure and temperature loading (red line). FE results are shown as black dash-dot lines.

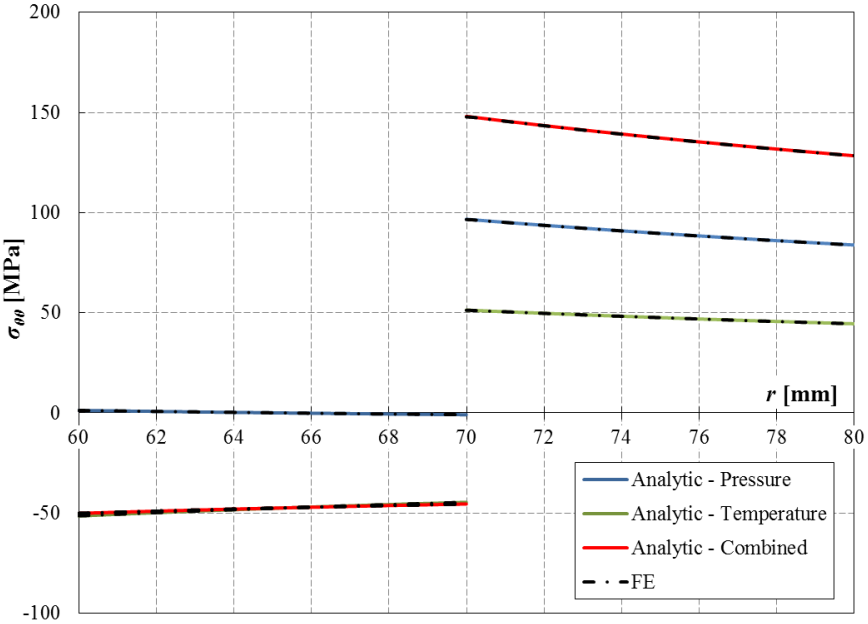

Figure B.6 – Analytically derived hoop stresses as a function of the radial coordinate *r* for configuration 2 (Table 1) in axially restrained condition with pressure loading (blue line), temperature loading (green line) and combined pressure and temperature loading (red line). FE results are shown as black dash-dot lines.

B.4 Configuration 2 - Axially Free

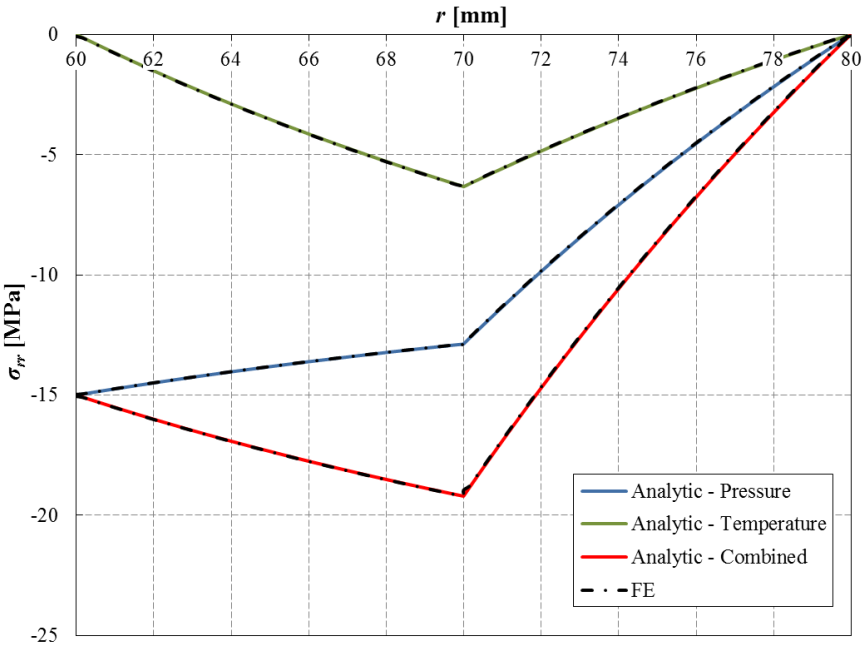

Figure B.7 – Analytically derived radial stresses as a function of the radial coordinate *r* for configuration 2 (Table 1) in axially free condition with pressure loading (blue line), temperature loading (green line) and combined pressure and temperature loading (red line). FE results are shown as black dash-dot lines.

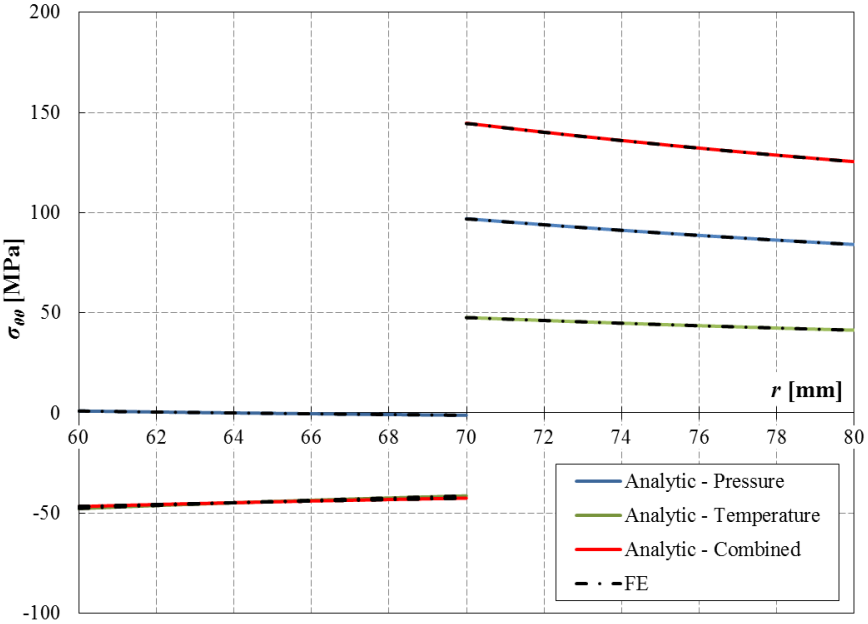

Figure B.8 – Analytically derived hoop stresses as a function of the radial coordinate *r* for configuration 2 (Table 1) in axially free condition with pressure loading (blue line), temperature loading (green line) and combined pressure and temperature loading (red line). FE results are shown as black dash-dot lines.

B.5 Configuration 2 – Spring-Mounted

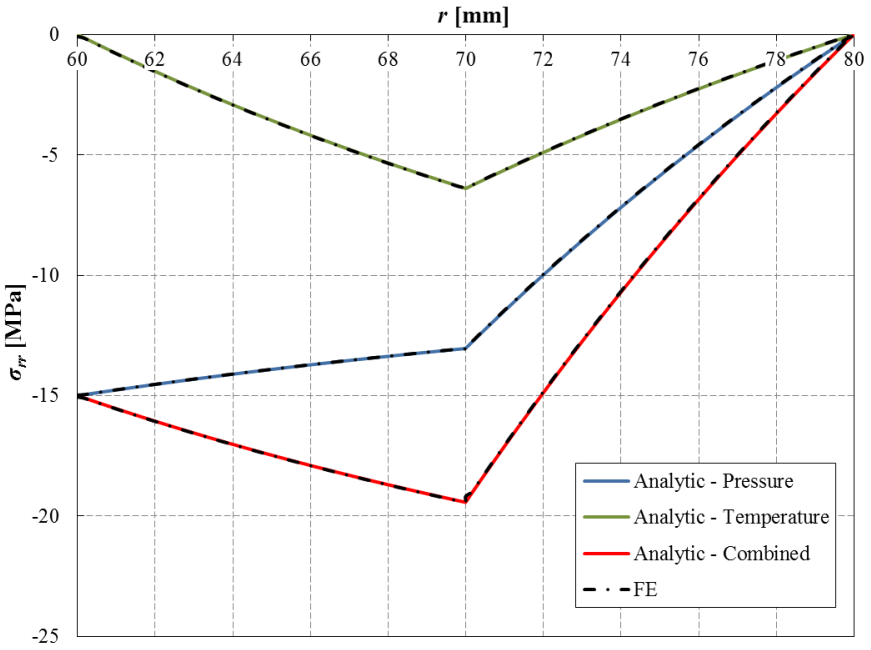

Figure B.9 – Analytically derived radial stresses as a function of the radial coordinate *r* for configuration 2 (Table 1) in spring-mounted condition with pressure loading (blue line), temperature loading (green line) and combined pressure and temperature loading (red line). FE results are shown as black dash-dot lines.

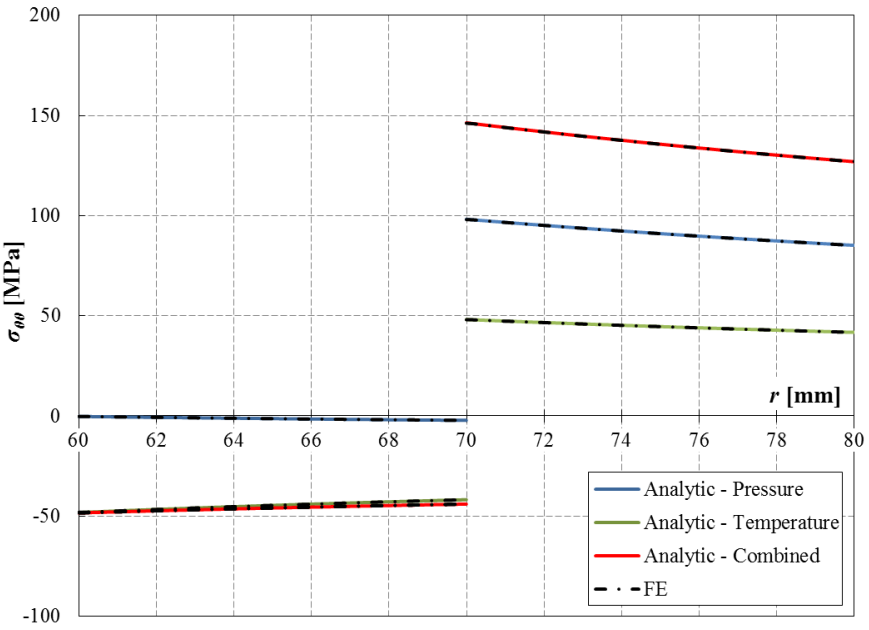

Figure B.10 – Analytically derived hoop stresses as a function of the radial coordinate *r* for configuration 2 (Table 1) in spring-mounted condition with pressure loading (blue line), temperature loading (green line) and combined pressure and temperature loading (red line). FE results are shown as black dash-dot lines.